Applied Surface Science 665 (2024) 160367

Contents lists available at ScienceDirect

Applied Surface Science

journal homepage: www.elsevier.com/locate/apsusc

Full Length Article

Al-Co-Cr-Fe-Ni high-entropy coatings produced by non-vacuum electron beam cladding: Understanding the effect of Al by in-situ synchrotron X-ray diffraction

T.S. Ogneva [a,*], K.I. Emurlaev [a], K.E. Kuper [b], N. Malyutina Yu [a], E.V. Domarov [b], I.K. Chakin [b], K.A. Skorokhod [c], A.A. Ruktuev [a], I.E. Nasennik [a], I.A. Bataev [a]

[a] Faculty of Mechanical Engineering and Technologies, Novosibirsk State Technical University, K. Marx Ave. 20, 630073 Novosibirsk, Russia
[b] Budker Institute of Nuclear Physics, Lavrentyev Ave. 11, 630090 Novosibirsk, Russia
[c] Khristianovich Institute of Theoretical and Applied Mechanics SB RAS, Institutskaya Str. 4/1, 630090 Novosibirsk, Russia

ARTICLE INFO

Keywords:
Non-vacuum electron beam cladding
High-entropy alloy
Coating
Synchrotron X-ray diffraction
Wear resistance
Hardness

ABSTRACT

This study investigates the structure and properties of Al-Co-Cr-Fe-Ni high-entropy alloy (HEA) based coatings on steel substrates produced by non-vacuum electron beam cladding. Powder mixtures with Al molar ratios of 0.5, 1, and 1.5 were used for cladding, resulting in coatings with fcc, bcc + fcc, and bcc structures, respectively. The Fe content, which entered the coating from the substrate during cladding, increased from 9.9 up to 48.1 at. % with the decrease of the Al molar fraction from 1.5 to 0.5. In-situ synchrotron X-ray diffraction analysis showed that this effect can be attributed to the higher solidus temperatures of the compositions with higher Al content. Electron backscatter diffraction showed that differences in grain morphology and crystallographic texture were related to the crystallization temperatures in different zones of the coatings. The bcc coating with an Al molar ratio of 1.5 demonstrated superior hardness and wear resistance. Fcc coating, which received more Fe from the substrate, had lower hardness and was prone to plastic flow. However, the specific wear rate of the fcc coating was close to that of the bcc + fcc one due to the hardening of the fcc phase during sliding wear.

1. Introduction

The concept of alloys consisting of multiple major elements, also known as high entropy alloys (HEAs), was introduced by Yeh in 2004 [1]. Since then, HEAs, specifically those of the Al-Co-Cr-Fe-Ni system, have garnered significant attention from the scientific community and have become one of the most intensively developed topics in materials science [1–5]. Al-Co-Cr-Fe-Ni-based HEAs alloys exhibit a unique combination of properties, including high hardness, strength, and ductility [6–12]. Furthermore, these alloys possess excellent wear resistance at both room and elevated temperatures [8,11,13,14], as well as high oxidation [6,10] and corrosion resistance [7,9]. These properties make Al-Co-Cr-Fe-Ni HEAs promising candidates for replacing NiAl-based intermetallic coatings, which are widely used as heat- and wear-resistant materials but have high brittleness at room temperature.

Currently, Al-Co-Cr-Fe-Ni-based coatings are often produced by arc or laser surfacing and plasma spraying [8,9,19,20,10,11,13–18]. These methods typically require a vacuum or a protective gas environment, increasing the complexity and cost. In this study, Al-Co-Cr-Fe-Ni coatings were produced using a non-vacuum electron beam cladding technique. This technique, known for its high performance, utilizes a high initial electron energy (1.4–2.4 MeV) to achieve coatings up to 2 mm thick in a single pass. However, there are only a few publications on obtaining HEA-based coatings using this method [6,21–23]. For today, electron-beam technologies are increasingly being used for 3D printing of products made of HEAs [24,25], or can be applied to change the structure and properties of the surface layers of bulk HEAs [26]. But, for such applications, the process takes place in vacuum chambers with lower energy levels compared to the technique demonstrated in this study.

The fabrication of the Al-Co-Cr-Fe-Ni coatings by non-vacuum electron beam cladding on steel typically implies that Fe is transferred into the coating from the substrate, which eliminates the need to add Fe to the initial powder mixture. This approach was previously successfully tested for the formation of HEA coatings in our previous studies [6,27].

The phase composition of the Al-Co-Cr-Fe-Ni coatings significantly

* Corresponding author.
E-mail address: ogneva@corp.nstu.ru (T.S. Ogneva).

https://doi.org/10.1016/j.apsusc.2024.160367
Received 7 March 2024; Received in revised form 11 May 2024; Accepted 21 May 2024
Available online 22 May 2024

depends on the molar ratio of the components, with Al acting as the strongest stabilizer of the bcc phase. Variations in Al content significantly affect the phase composition, structure, and properties of the alloys in this system [28–33]. Taking this into account, it is hypothesized that the Al content during non-vacuum electron beam cladding of Al-Co-Cr-Fe-Ni HEAs on steel substrates could impact the transfer of Fe from the substrate to the cladded layer, ultimately affecting the formation process of coatings. While this hypothesis may not be immediately apparent, this study will demonstrate that such an effect does indeed exist and has a significant impact on the structure and properties of coatings. Currently, there is a lack of research in the scientific literature addressing this specific issue.

The aim of this study was to investigate the effect of Al content on the structure, phase composition, and mechanical properties of Al-Co-Cr-Fe-Ni coatings obtained by non-vacuum electron beam cladding of Al, Co, Cr, and Ni powders on steel substrates.

2. Materials and methods

2.1. Production of coatings

Experiments on non-vacuum electron-beam cladding were performed at the UNU Stand ELV-6 industrial electron accelerator facility (BINP SB RAS, Novosibirsk). This facility offers a high initial energy of electrons ranging from 1.4 to 2.4 MeV, which provides deep penetration of the electron beam in solid materials, allowing for the cladding of layer thicknesses ranging from 0.5 to 2 mm in a single pass. The electron beam passes through a multi-chamber vacuum system and is injected into a regular air atmosphere. This unique feature significantly simplifies the cladding process and reduces manufacturing costs.

The diameter of the beam at the outlet of the electron accelerator was initially 1 mm. The distance from the outlet to the sample was 90 mm. As the beam traveled through this distance, it scattered in the air atmosphere, increasing its diameter to 12 mm. During cladding, the table with the sample moved under the beam at a constant speed, while an electromagnetic scanning system deflected the electron beam in the transverse direction at a frequency of 50 Hz to increase the width of the processed area. In this study, the beam was deflected from the vertical axis by an angle of ±21°, allowing the processing of 50-mm-wide samples in a single pass. A detailed description of the ELV-6 accelerator and the results of typical experiments are provided elsewhere [6,21].

The cladding parameters shown in Table 1 were selected based on preliminary experiments. These parameters ensured the formation of smooth, uniform coatings for all compositions of the powder mixtures used in this study.

Three different powder mixtures, each containing a different amount of Al, were used for the cladding:

- composition with equal molar ratios of Al, Co, Cr, and Ni;
- composition with an Al molar ratio of 0.5 and Co, Cr, and Ni molar ratios of 1;
- composition with an Al molar ratio of 1.5 and Co, Cr, and Ni molar ratios of 1.

Commercially pure Co and Cr powders and intermetallic NiAl powder were used to prepare the powder mixtures. Low-carbon steel (0.2 wt% C, 0.25 wt% Cr, 0.28 wt% Si, 0.55 wt% Mn) plates with dimensions of 100 × 50 × 20 mm^3 were used for the substrates. One may notice that Fe was not included in the powder mixture. During electron beam cladding, the substrate material will inevitably enter the coating when the surface layer of the steel substrate is melted and mixed with the molten powders. Besides, HEAs don't require much Fe in their compositions, thus, the better way is to receive it from the substrate without adding to the powder mixture. If needed, the amount of Fe can be varied by varying the energy density of the electron beam. To prepare the composition with a molar ratio of Al = 1.5, pure Al powder was added to the powder mixture. To obtain a composition with a molar ratio of Al = 0.5, the amount of other powders in the mixture was increased accordingly.

Table 1
Parameters of non-vacuum electron beam cladding.

Mass of metal powders*, (g)	Mass of flux *, (g)	Current, mA	Table velocity, (mm/s)	Mass of powder mixture (metal + flux) per unit area (g/cm^2)	Energy density (kJ/cm^2)
15.75	7.2	25	15	0.45	4.67

* Mass distributed over the entire area of the substrate 100 × 50 mm^2.

Flux was added to the powder mixture to dissolve oxide films and protect the melt pool from oxidation. The content of flux was 32 wt% of the total mass of the powder mixture. Because of its low density, the flux floated up when melted and solidified on the coating surface as a slag crust, which was easily removed mechanically. Based on the recommendations presented in [34], a mixture of 50 wt% Ca_2F and 50 wt% LiF powders was selected as the flux material. According to [34], the working temperature range of the flux should be within the melting and boiling points of the most easily melting component. Ca_2F (melting temperature 2527 °C) provides an effective dissolution of oxide films on steel substrates. Additions of LiF due to its low melting temperature (849 °C) helps prevent the spitting of melted Al in compositions that contain Al powder.

2.2. Characterization methods

The structure of the samples was studied in a cross-section. The samples were cut using a Struers Discotom-65 disk cutting machine and ground using abrasive papers ranging from P300 to P2500. Subsequently, they were polished using diamond (particle size of 9–1 μm), aluminum oxide (particle size of 0.3 μm) and silica (particle size of 0.05 μm) suspensions. A solution consisting of 25 % nitric acid, 25 % hydrofluoric acid, and 50 % water was used for etching. The microstructure was characterized using a Carl Zeiss Axio Observer Z1m light microscope (LM) and a Carl Zeiss EVO 50 XVP scanning electron microscope (SEM) equipped with an Oxford Instruments X-Act energy dispersive X-ray (EDX) spectrometer. EDX analysis was used to measure the average content of elements in the samples and the local composition of transition zones at the "coating-substrate" interface and in the local points of the coating. Average composition was found by 5 measurements in rectangular regions with an area of ~0.5 mm^2 each. The composition of local zones was measured in 5 points for each characteristic zone of the coating. The measurement errors were calculated using a confidence interval with a statistical significance level of 0.05. The grain structure after etching was studied using a Carl Zeiss Sigma 300 SEM with an Inlens Duo detector.

Electron backscatter diffraction (EBSD) analysis was performed using a Carl Zeiss Sigma 300 microscope equipped with an Oxford Instruments HKL Channel 5 detector. Specimens for EBSD analysis were prepared by mechanical grinding using sandpaper, followed by polishing using diamond suspensions of 9, 6, 3 and 1 μm, and 0.3 μm silica suspension. The final preparation step was 1.5 h of polishing with a QPol Vibro vibratory polisher (SAPHIR VIBRO) using a 0.05 μm colloidal silica suspension.

The phase composition of the samples was found by synchrotron X-ray diffraction (SXRD). Experiments using synchrotron radiation were carried out at 8-A beamline of the VEPP-4 source at the Shared Use Center SCST (BINP SB RAS, Novosibirsk). The 0.5-mm-thick samples were cut from the cladded layer by wire discharge machining and examined in transmission mode. The photon energy was 69.5 keV, which corresponded to a wavelength of 0.1783 Å. The beam size was 200 × 200 $μm^2$, the distance from the sample to the detector was 473.8

mm. Diffraction patterns were recorded using a Mar345 detector (resolution 3500 × 3500 pixels, pixel size 100 × 100 μm^2) with an exposure time of 2 min per pattern. Two-dimensional diffraction rings were azimuthally integrated, and analyzed as typical "Intensity – Scattered angle 2θ" powder diffraction patterns.

In-situ high-temperature SXRD studies were performed to estimate the temperature of liquid phase formation during heating. A halo appeared in annular diffraction patterns when the liquid phase appeared during heating. For this experiment, the radiation energy was 49,87 keV, the wavelength was 0.2480 Å, the beam size was 200 × 200 μm^2, the distance from the sample to the detector was 286.65 mm. Diffraction patterns were recorded by a Mar345 detector with an exposure time of 2 min. The size of the specimens was 5 × 5 mm^2, and the thickness was 0.5 mm. The experiment was carried out in an argon atmosphere. Heating was performed using an ytterbium fiber laser with a maximum power of 527 W. The temperature of the sample was measured using a thermal imaging camera. The accuracy of the temperature estimation was ± 25 °C. The obtained annular diffraction patterns were azimuthally integrated, and the "Temperature – Scattered angle 2θ" intensity maps were built. The scheme of the experiment and a typical two-dimensional diffraction pattern showing the appearance of a halo above the solidus temperature are shown in Fig. 1.

Vickers microhardness was measured using a Wolpert Group 402MVD instrument. The measurements were carried out in a cross-section in the direction from the top of the cladding layer toward the substrate. The load on the indenter was 0.98 N. The distance between the indentations was 100 μm.

Dry sliding wear tests with reciprocating motion were performed using a universal friction machine Bruker Nano GmbH UMT-2 at room temperature using a "ball-plane" scheme with a non-rotating ball. WC balls of 6.35 mm in diameter were used as a counterbody. Before the tests, the surface of the coatings was prepared according to a traditional sample preparation technique, including grinding on abrasive paper and diamond suspensions and polishing to a mirror finish using a colloidal silica suspension. The tests were carried out in the following modes: movement length was 5 mm, movement frequency was 5 Hz; load applied on the counterbody was 25 N; and the total sliding distance was 100 m. The wear surface was examined using a Carl Zeiss EVO 50 XVP scanning electron microscope. The volume of the worn material was determined using a Bruker Nano GmbH Contour GT-K1 optical profilometer.

3. Results and discussion

3.1. Microstructure of the coatings

3.1.1. Elemental composition and phase constitution of the coatings

Table 2 lists the elemental compositions of the initial powder mixtures before cladding, the average element composition of the samples after the cladding, and the corresponding molar ratios of the elements in the coatings. For convenience, the samples will be designated hereafter according to the stoichiometric ratio of the elements measured after the cladding.

The thickness of the coatings varied with the amount of Al. The coatings with a molar ratio of Al = 1 and 1.5 were ~600 μm thick, and the coatings with a molar ratio of Al = 0.5 were ~900 μm thick. EDX analysis showed that the molar ratio of Al, Co, Cr, and Ni in the cladded layers approximately corresponded to the initial ratio of these elements in the powder mixtures; however, the amount of Fe entered from the substrate differed significantly. AlCoCrFe$_{0.6}$Ni sample, which was produced with an equal molar ratio of elements in the initial powder mixture, contained approximately 12.8 at. % Fe. In coatings with an excess of Al (Al$_{1.5}$CoCrFe$_{0.5}$Ni), the Fe concentration was slightly lower at around 9.9 at. %, and in coatings with a lack of Al in a powder mixture (Al$_{0.5}$CoCrFe$_{3.2}$Ni), the Fe content significantly increased to 48.1 at. %.

A small amount of carbon, as well as Cr, Mn and Si (i.e. the alloying elements of the low carbon steel, which was used for the substrates), entered the coating during the process of cladding. EDX analysis didn't reveal any amount of Mn in the main part of the AlCoCrFe$_{0.6}$Ni and Al$_{1.5}$CoCrFe$_{0.5}$Ni samples, 0.6 at. % of Si was detected in the AlCoCrFe$_{0.6}$Ni sample, and 0.5 at. % of Si in the Al$_{1.5}$CoCrFe$_{0.5}$Ni sample. In Al$_{0.5}$CoCrFe$_{3.2}$Ni sample, Si content was 0.7 at. % and Mn content was 0.2 at. %. The amount of carbon can't be estimated quantitatively by EDX analysis, but it was also detected in a very small amount in the interdendritic regions of the samples AlCoCrFe$_{0.6}$Ni and Al$_{1.5}$CoCrFe$_{0.5}$Ni, and in the FCC phase of the Al$_{0.5}$CoCrFe$_{3.2}$Ni sample. As the amount of C, Si and Mn was very small, it didn't influence the phase constitution, structure, and properties of the alloys. The amount and distribution of alloying elements entering the coating from the low-carbon steel substrate were also evaluated more precisely in our previous publications devoted to cladding of NiAl-based alloys [23] and annealing of AlCoCrFeNi HEAs [27].

SXRD analysis showed that the sample with an equiatomic ratio of the initial components in the powder mixture (AlCoCrFe$_{0.6}$Ni) consisted of bcc and fcc phases. The Al$_{1.5}$CoCrFe$_{0.5}$Ni sample predominantly contained the bcc phase (Fig. 2a); however, upon a more precise analysis, faint fcc phase reflections were also noticed (Fig. 2b and c). Thus, it can be concluded that a very small volume fraction of the fcc phase was present in this sample. The bcc phase displayed additional superstructural reflections, suggesting the formation of an ordered B2 structure. The formation of disordered A2 + ordered B2 structures is a common fact for Al-Co-Cr-Fe-Ni-based HEAs [28,30,32,35]. The Al$_{0.5}$CoCrFe$_{3.2}$Ni sample obtained with an Al deficiency in the powder mixture was found to consist of a single fcc phase.

The tendency of HEAs to form bcc or fcc structures depends on the valence electron concentration (VEC). Research by Guo et al. [36]

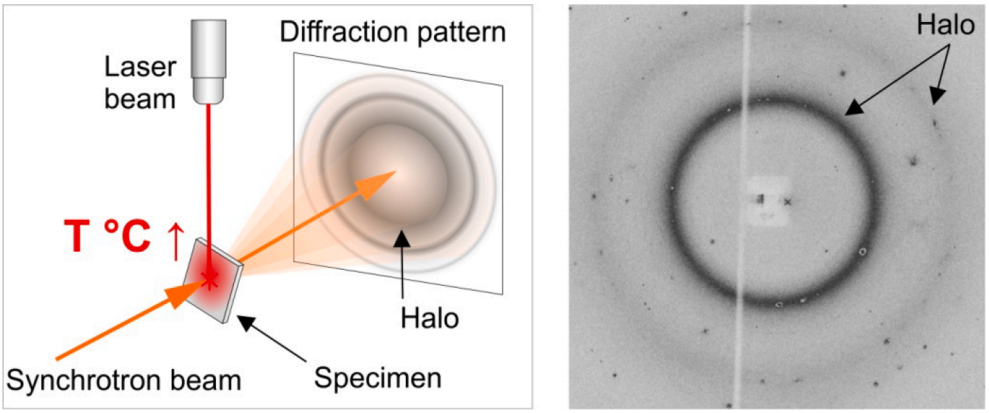

Fig. 1. The scheme of the experiment (a), and an annular diffraction pattern with a halo, obtained when heating the sample above the solidus temperature (b).

Table 2
The composition of the powder mixtures used for the cladding and the average elemental composition of the samples after the cladding measured by EDX analysis.

Molar ratio of Al relative to other elements	Nominal composition of the powder mixture before cladding				Composition of the cladded layer					Stoichiometric composition (Sample designation)
	Al at. %	Co at. %	Cr at. %	Ni at. %	Al at. %	Co at. %	Cr at. %	Fe at. %	Ni at. %	
1	25	25	25	25	21.1 ± 1.2	22.0 ± 0.5	22.1 ± 1.1	12.8 ± 0.6	22.0 ± 0.5	$AlCoCrFe_{0.6}Ni$
1.5	33.3	22.2	22.2	22.2	29.2 ± 1.5	20.3 ± 0.4	20.4 ± 1.3	9.9 ± 0.7	20.2 ± 0.5	$Al_{1.5}CoCrFe_{0.5}Ni$
0.5	14.2	28.6	28.6	28.6	7.0 ± 0.7	15.1 ± 0.5	15.0 ± 0.8	48.1 ± 2.2	14.8 ± 0.4	$Al_{0.5}CoCrFe_{3.2}Ni$

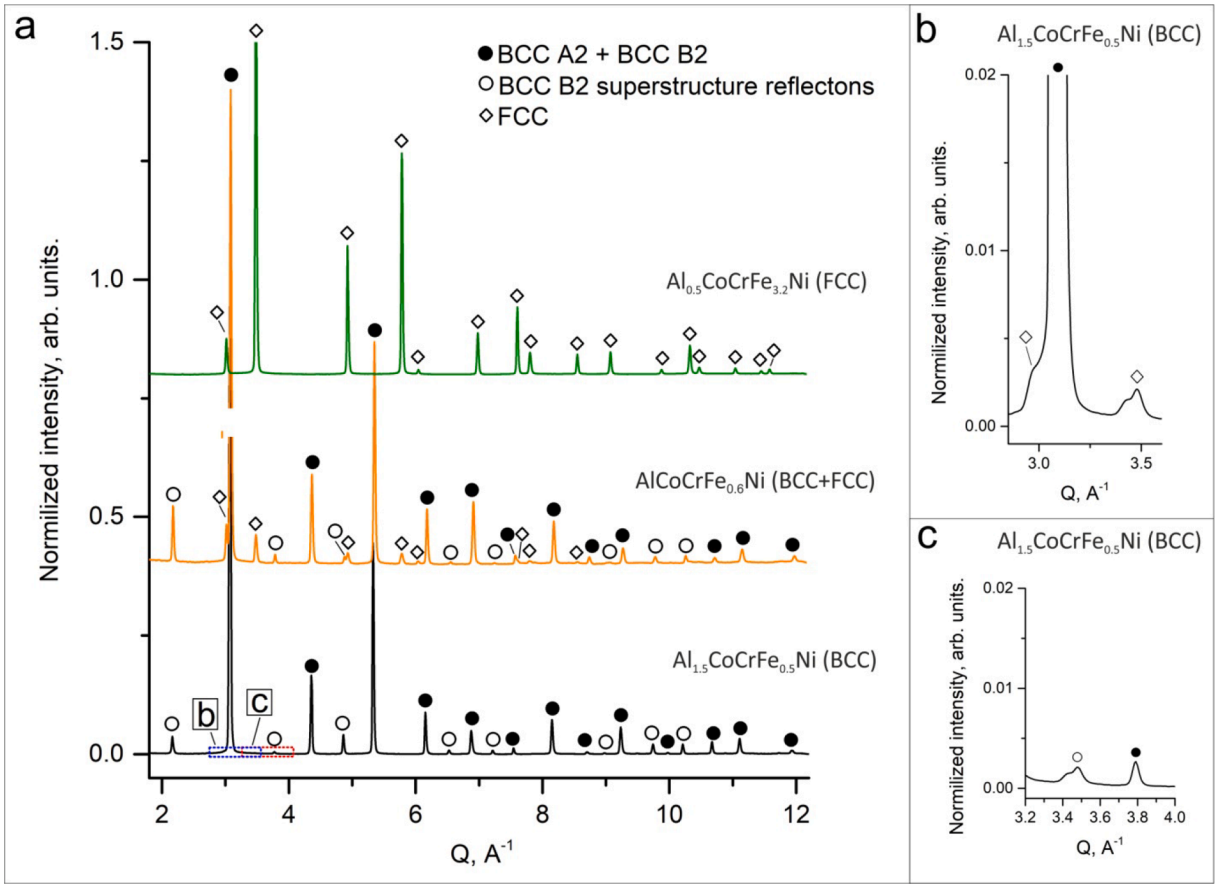

Fig. 2. SXRD patterns of the Al-Co-Cr-Fe-Ni coatings produced by non-vacuum electron beam cladding.

showed that alloys with VEC ≥ 8.0 tend to adopt an fcc structure, a bcc structure is formed when VEC ≤ 6.87, and for intermediate VEC values ranging from 6.87 to 8, two-phase bcc + fcc alloys should exist. Different studies may slightly vary on the exact VEC values for single-phase bcc and fcc regions, but the overall trend remains consistent. For instance, according to Tian et al. [37], the regions of single bcc and fcc phases formation correspond to VEC ≤ 7.04 and VEC ≥ 7.57, respectively. In the Al-Co-Cr-Fe-Ni system, Al has the lowest VEC value at 3 electrons per atom, making it the strongest stabilizer of the bcc phase. As a result, in Al-Co-Cr-Fe-Ni HEAs, Al has the greatest effect on the value of VEC.

The VEC values calculated from the EDX data in this study are summarized in Table 3. The phase constitution of the samples agrees with the criterion described above. Specifically, $Al_{0.5}CoCrFe_{3.2}Ni$ sample exhibited the highest VEC value of 7.80, resulting in the formation of an fcc phase. The sample $Al_{1.5}CoCrFe_{0.5}Ni$ with the lowest VEC value of 6.74 predominantly consisted of a bcc phase. $AlCoCrFe_{0.6}Ni$ sample, with an intermediate VEC value of 7.16 possessed a two-phase bcc + fcc

Table 3
VEC values calculated for the samples.

Sample	Phase composition of the coatings	VEC (electrons per atom)
$Al_{0.5}CoCrFe_{3.2}Ni$	fcc	7.80
$AlCoCrFe_{0.6}Ni$	bcc + fcc	7.16
$Al_{1.5}CoCrFe_{0.5}Ni$	Predominantly bcc + small amount of fcc	6.74

structure. It is important to note that most literature sources report VEC values corresponding to the equilibrium state of the alloys, whereas the coatings in this work crystallized under conditions of rapid heat removal toward the substrate. Therefore, quantitative correlations between phase composition and VEC values should be interpreted with caution.

The different Fe content in the samples can be explained as follows. When cladding, before Fe started to transfer into the just-melted

coatings, their composition corresponded to the nominal ratios $Al_{0.5}CoCrNi$, AlCoCrNi, and $Al_{1.5}CoCrNi$. As mentioned above, as the amount of Al in the alloy increases, the likelihood of forming a bcc phase also increases, whereas the likelihood of forming an fcc phase decreases. The data of Saha et al. [38] indicate that the $Al_{0.5}CoCrNi$ alloy has a liquidus temperature of ~1380 °C and regularly crystallizes in the fcc phase. Phase diagrams proposed by G. Zhang et al. [39] and Ostrowska et al. [40] suggested that the AlCoCrNi alloy has a bcc crystal lattice and a higher liquidus temperature of approximately 1465 °C. Information on melting temperatures for the $Al_{1.5}CoCrNi$ alloy was not found in the literature. Nevertheless, as can be seen from the calculated phase diagrams of most systems, such as Al-Fe-Ni, Al-Co-Ni, Al-Cr-Ni [41–44], Al-Co-Cr-Fe-Ni [25,39,40,45,46], the melting temperature of the Al-rich bcc B2 phase is usually 150–300 °C higher than that of the Al-depleted disordered fcc phase. This temperature range can vary depending on the elemental composition and stoichiometry.

For this reason, when cooling down the Al-rich liquid alloys, which are prone to the formation of bcc B2 structure, crystallization begins at higher temperatures (about 1500–1600 °C) compared with Al-depleted compositions. Therefore, other things being equal, Al-rich samples spend less time in the molten state and don't have enough time to dissolve a large amount of Fe from the substrate. Conversely, if there is a lack of Al, the coating remains in the liquid state longer, and a significant amount of Fe from the steel substrate has time to transfer into the coating.

Fe, which is introduced into the coatings from the substrate, can also impact the crystallization temperature of the samples. According to the literature data, $AlCoCrFe_xNi$ alloys with a lower Fe concentration have a larger volume fraction of the bcc phase and higher melting temperatures. For instance, according to the calculated $AlCoCrFe_xNi$ phase diagrams presented by G. Zhang et al. [39] and Ostrowska et al. [40], when the molar fraction of Fe decreases from 1 to 0, the melting temperature of the alloy increases from the range of 1350–1400 °C to 1440–1465 °C. According to the calculations given in [39], in $AlCoCrFe_xNi$ alloys x = 3, the melting point notably lower at around 1330 °C.

The effect of changing the concentration of two elements simultaneously (Al and Fe) on the melting temperature of HEAs is difficult to assess without experimental studies. To address this issue, phase transformations in the coatings near solid–liquid phase transition temperatures were studied using in-situ SXRD analysis Furthermore, EBSD analysis was performed to better understand the process of coating crystallization. The results of these studies are detailed in the subsequent sections.

3.1.2. SXRD analysis of coatings during heating

A visual representation of phase transformations during heating for each sample is shown in the colored map (Fig. 3). Each point of this map represents the intensity of the scattered X-ray radiation at the corresponding 2θ angle during heating. The data obtained were compared with the results of calculations previously published by other researchers (Table 4), [25,39,40,45–48]. It should be considered that the samples analyzed in this study may vary slightly in composition compared with the samples studied by other researchers. However, a joint analysis of theoretical and experimental data allows understanding how phase transition temperatures shift with variations in Al and Fe content. Let us now delve into the results obtained for each of the three samples individually.

3.1.2.1. $AlCoCrFe_{0.6}Ni$ sample. When heating the $AlCoCrFe_{0.6}Ni$ sample, the formation and dissolution of the σ-phase were observed in the

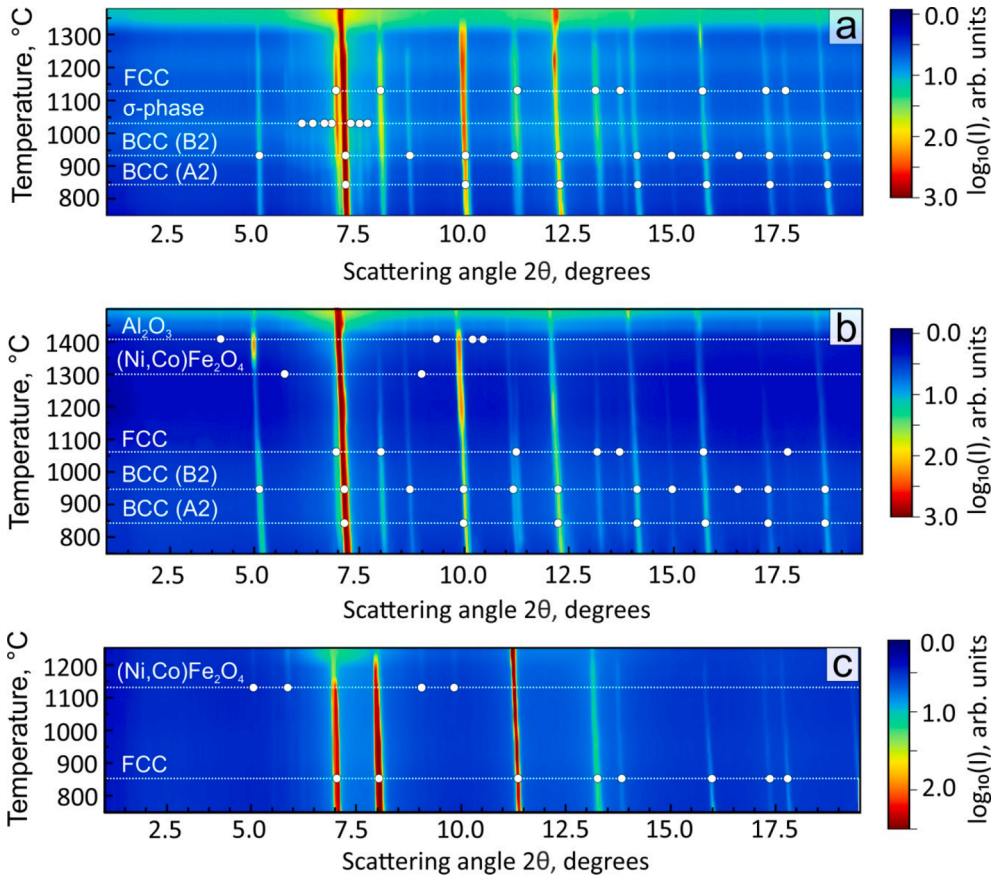

Fig. 3. Heating maps of $AlCoCrFe_{0.6}Ni$ (a), $Al_{1.5}CoCrFe_{0.5}Ni$ (b), and $Al_{0.5}CoCrFe_{3.2}Ni$ (c) samples obtained by SXRD. White circles are used to mark the diffraction maxima at the corresponding phases.

Table 4
The solidus and liquidus temperatures for the $AlCoCrFe_{0.6}Ni$, $Al_{0.5}CoCrFe_{3.2}Ni$, and $Al_{0.5}CoCrFe_{3.2}Ni$ samples estimated in this work by SXRD, and the data for alloys with similar compositions obtained by other researchers.

Composition	Approximate solidus temperature, °C	Approximate liquidus temperature, °C	Method	Reference
$AlCoCrFe_{0.6}Ni$	1275	above 1375	SXRD	This work
$Al_{1.5}CoCrFe_{0.5}Ni$	1425	above 1500		
$Al_{0.5}CoCrFe_{3.2}Ni$	1200	above 1250		
$Al_{0.5}CoCrNi$	1350	1380	Thermodynamic calculations	[38]
AlCoCrNi	1340	1440		[39]
	1315	1465		[40]
$AlCoCrFe_{0.6}Ni$	1280	1380	Thermodynamic calculations	[39]
	1315	1210		[46]
	1250	1430		[40]
$Al_{1.5}CrCoFeNi$	1430	1470	Thermodynamic calculations + DSC	[45]
	1420	1500	Thermodynamic calculations	[40]
	1320	1460		[25]
	1180	1390		[46]
$AlCoCrFe_3Ni$	1290	1330	Thermodynamic calculations	[39]

temperature range of 750–1025 °C (Fig. 3a). Furthermore, the intensity of the fcc reflections increased in this sample in the temperature range of 900–1275 °C. These structural changes during heating occurred due to the fact that the coating material after cladding was rapidly cooled, leading to its crystallization in a highly nonequilibrium state. The precipitation of the σ-phase upon heating in bcc + fcc Al-Co-Cr-Fe-Ni alloys usually occurs up to 1000 °C [39,40]. The appearance of the fcc phase in bcc Al-Co-Cr-Fe-Ni HEAs is often observed during the annealing of samples produced under nonequilibrium conditions, for instance, by gas atomization [42,49,50] or mechanical activation [31].

The heating of the alloy above the solidus temperature and the formation of a liquid phase can be detected through the appearance of a halo in the diffraction patterns. In $AlCoCrFe_{0.6}Ni$ sample, which predominantly consisted of the bcc phase and a certain amount of the fcc phase, the first signs of melting became noticeable at 1275 °C. At this temperature, the intensity of fcc significantly decreased, indicating its melting (Fig. 3a). The volume fraction of fcc inclusions in the bcc matrix of the $AlCoCrFe_{0.6}Ni$ sample wasn't large, therefore, when the fcc phase melted, no noticeable blurring of reflections or halo were observed. A bright halo appeared when the temperature reached 1300 °C, which indicated the melting of a significant portion of this sample. Apparently, the melting of bcc A2 phase began at this temperature. Y. Zhang et al. [46] and G. Zhang et al. [39] found that the bcc A2 phase becomes liquid at temperatures approximately 40–60 °C higher than the melting point of the fcc phase. It should be noted that there are very few publications on the phase diagrams of $AlCoCrFe_xNi$ alloys, and the existing publications show discrepancies. Moreover, the authors of this study were unable to find in the literature any experimental data on the solidus and liquidus temperatures of $AlCoCrFe_xNi$ alloys, such as data from differential scanning calorimetry. As a result, it is challenging to speculate which of the known versions of the existing $AlCoCrFe_xNi$ phase diagram is more accurate and suitable for comparison with our experiment. Therefore, we have chosen to compare our results with various existing literature data. According to the phase diagram reported in [39], the melting temperatures of the fcc and bcc A2 phases are approximately 1280 and 1310 °C, respectively, whereas in [46], these temperatures are around 1210 and 1270 °C. In contrast, the diagram calculated in [40] predicts a different order of phase melting, with the bcc A2 phase turning into a liquid state at ~1250 °C followed by fcc melting at ~1310 °C. The temperatures and melting sequences of the fcc and bcc A2 phases observed experimentally in the present study are close to the data reported in [46] and [39].

During heating, weak reflections of the $(Ni,Co)Fe_2O_4$ and Al_2O_3 oxides were also observed in the diffraction patterns. Apparently, a small amount of these compounds was formed on the surface of the specimens as they were subjected to high temperatures during the in-situ SXRD experiment. Thin films containing $(Ni,Co)Fe_2O_4$ and Al_2O_3 phases are usually formed on Al-Co-Cr-Fe-Ni HEAs during high-temperature oxidation [27,51–56].

3.1.2.2. $Al_{1.5}CoCrFe_{0.5}Ni$ sample. At room temperature, the reflections of the fcc phase were poorly visible in the diffraction pattern of the $Al_{1.5}CoCrFe_{0.5}Ni$ sample, but their intensity increased significantly in the temperature range from 775 to 1100 °C (Fig. 3b). With further heating, the fcc phase in the $Al_{1.5}CoCrFe_{0.5}Ni$ coating gradually decomposed and almost completely disappeared at 1375 °C.

The sample began to melt at 1425 °C (Fig. 3b). This approximately corresponds to the solidus temperature of the $Al_{1.5}CrCoFeNi$ alloy according to the calculations carried out by Stryzhyboroda et al. [45] and Ostrowska et al. [40] and is around 100 °C higher than the data reported by Kuwabara et al. [25]. The SXRD data in Fig. 3b indicated that even when the temperature was increased up to 1500 °C, the liquidus temperature of the $Al_{1.5}CoCrFe_{0.5}Ni$ sample hadn't yet been reached. Usually, at this temperature, only the B2 bcc phase remains in the crystalline state in AlCoCrFeNi-based alloys because of its high melting point. According to [25,40,45], the compound $Al_{1.5}CrCoFeNi$ completely transforms into a liquid state in a range of 1460–1500 °C. A possible reason why the $Al_{1.5}CoCrFe_{0.5}Ni$ sample didn't melt at 1500 °C might be the low Fe content. According to the calculated data of other researchers, the lack of Fe in $Al_xCrCoFeNi$ alloys [39,40,46] and the excess of Al in the $Al_xCrCoFeNi$ alloys [25,40,45] lead to a higher volume fraction of the B2 bcc phase and contribute to raising the melting point of the alloys.

3.1.2.3. $Al_{0.5}CoCrFe_{3.2}Ni$ sample. The onset of melting in the $Al_{0.5}CoCrFe_{3.2}Ni$ sample was observed at 1200 °C, as indicated by the formation of a halo and a sharp decrease in the intensity of nearly all fcc reflections (Fig. 3c). According to the $AlCoCrFe_xNi$ phase diagram reported by G. Zhang et al. [39], the solidus temperature of the alloy with $x = 3$ is approximately 1290 °C. The solidus temperature for the $Al_{0.5}CoCrFe_{3.2}Ni$ sample observed in this study is lower than that calculated in [39] for close stoichiometry $AlCoCrFe_3Ni$. However, due to the lower Al content in $Al_{0.5}CoCrFe_{3.2}Ni$, the solidus temperature may differ. Considering the effect of Fe, the solidus temperature 1350 °C of the composition $Al_{0.5}CoCrNi$ calculated in [38] was ~150 °C lower than that for $Al_{0.5}CoCrFe_{3.2}Ni$. This suggests that the gradual transfer of Fe during cooling of the coating led to a gradual reduction of the solidus temperature, and finally the alloy crystallized when 48.1 at.% of Fe dissolved in the cladded layer during this process.

Thus, SXRD analysis revealed that the $AlCoCrFe_{0.6}Ni$ sample was in a liquid state in the temperature range 1275–1375 °C, the $Al_{1.5}CoCrFe_{0.5}Ni$ sample – in the range 1425–1500 °C, and $Al_{0.5}CoCrFe_{3.2}Ni$ sample – in the range 1200–1250 °C. The data obtained showed that the temperatures of liquid phase formation in the $Al_{0.5}CoCrFe_{3.2}Ni$ sample were the lowest. Although the design of the experiment didn't allow the recording of diffraction patterns at temperatures as close as possible to the liquidus temperature, and the accuracy of temperature estimation

(±25 °C) didn't allow the determination of the phase transitions temperatures with an accuracy of a degree, the data obtained were sufficient for a relative assessment of the difference in melting temperatures and for confirmation of the hypothesis explaining the difference in Fe content in the cladded samples.

3.1.3. Microstructure of the coatings

The two-phase bcc + fcc $AlCoCrFe_{0.6}Ni$ sample had a dendritic structure, which is typical for crystallization from a liquid state. The body of the dendrites was a bcc phase, and the fcc phase was predominantly distributed in the interdendritic space, having the shape of discontinuous thin layers less than 2 μm thick (Fig. 4a–c).

The results of local EDX analysis of the dendritic and interdendritic areas presented in Table 5 showed that the bcc phase was enriched in Al and Ni, and the fcc phase was enriched in Fe and Cr (Fig. 4b). Co was distributed fairly evenly throughout the sample. Other elements were noticeably segregated inside the bcc grains. In the center of the dendritic crystals, the concentrations of Al and Ni were higher, while regions with increased Fe and Cr concentrations were located closer to the fcc zones. Etching of the $AlCoCrFe_{0.6}Ni$ sample revealed the segregation of the bcc phase with the precipitation of a nanosized mixture of A2 and B2 structures (Fig. 4d–f), which often appears in AlCoCrFeNi HEAs as a result of spinodal decomposition [28,30]. In the center of the dendritic branches, fine spherical nanoprecipitates approximately 50 nm in size were formed (Fig. 4d), while closer to the edges of the dendrites, a nanosized structure of braided wavy morphology was revealed with a thickness of elements ~70 nm (Fig. 4e). In some areas near the edges of the bcc grains, these precipitates had a labyrinth-like shape (Fig. 4f) elongated in the direction of crystallization and mixing with zones of spherical nanoprecipitates. The center of the dendrites in the $AlCoCrFe_{0.6}Ni$ sample contained more Al and Ni; therefore, it can be concluded that the lighter, less etched particles in Fig. 4c–e most likely corresponded to the A2 structure, and the darker, well-etched areas corresponded to the B2 structure. The morphology of A2 + B2 structure in the center and at the periphery of the dendrites may differ due to significant chemical heterogeneity. As a result, the periphery of the dendritic grains was depleted in Al, and the volume fraction of the A2 structure was presumably higher closer to the dendritic boundaries.

Table 5
EDX analysis of local zones of the coating.

Element	$AlCoCrFe_{0.6}Ni$			$Al_{1.5}CoCrFe_{0.5}Ni$		
	DR center	DR edge	ID	DR center	DR edge	ID
Al, at. %	29.2 ± 2.7	20.2 ± 3.3	11.0 ± 3.4	39.9 ± 3.6	34.2 ± 3.9	18.5 ± 5
Cr, at. %	14.8 ± 1.8	22.7 ± 4.1	29.8 ± 5.6	9.7 ± 2	17.6 ± 5.2	36.7 ± 7.3
Fe, at. %	6.3 ± 0.7	12.5 ± 2.9	15.3 ± 4.7	5.8 ± 3.2	9.3 ± 0.7	11.8 ± 1
Co, at. %	21.5 ± 0.5	22.1 ± 1.5	23.8 ± 2.7	17.9 ± 0.2	18.4 ± 0.3	18.4 ± 0.7
Ni, at. %	28.2 ± 0.5	22.5 ± 2.0	20.1 ± 2.7	26.7 ± 1.4	20.5 ± 1.2	13.4 ± 2.1

DR – dendritic region, ID – interdendritic region

(a) dendritic structure after etching, (b) dendritic structure before etching, areas of local EDX analysis are marked with arrows (Table 5), (c) structure with bcc and fcc regions after etching; (d) bcc region with a high content of Al, and Ni, (e,f) bcc region with a high content of Cr and Fe.

The $Al_{1.5}CoCrFe_{0.5}Ni$ sample consisted predominantly of the bcc phase and had a dendritic structure similar to that of the $AlCoCrFe_{0.6}Ni$ sample. A similar segregation of elements with increased Ni and Al contents in the center of the dendrites and increased Cr and Fe contents closer to the boundaries of the dendritic branches was observed (Table 5, Fig. 5a and b).

In contrast to the previously discussed $AlCoCrFe_{0.6}Ni$ sample, the $Al_{1.5}CoCrFe_{0.5}Ni$ sample showed a lack of fcc phase precipitation in the interdendritic regions, likely due to the higher Al content. The A2 + B2

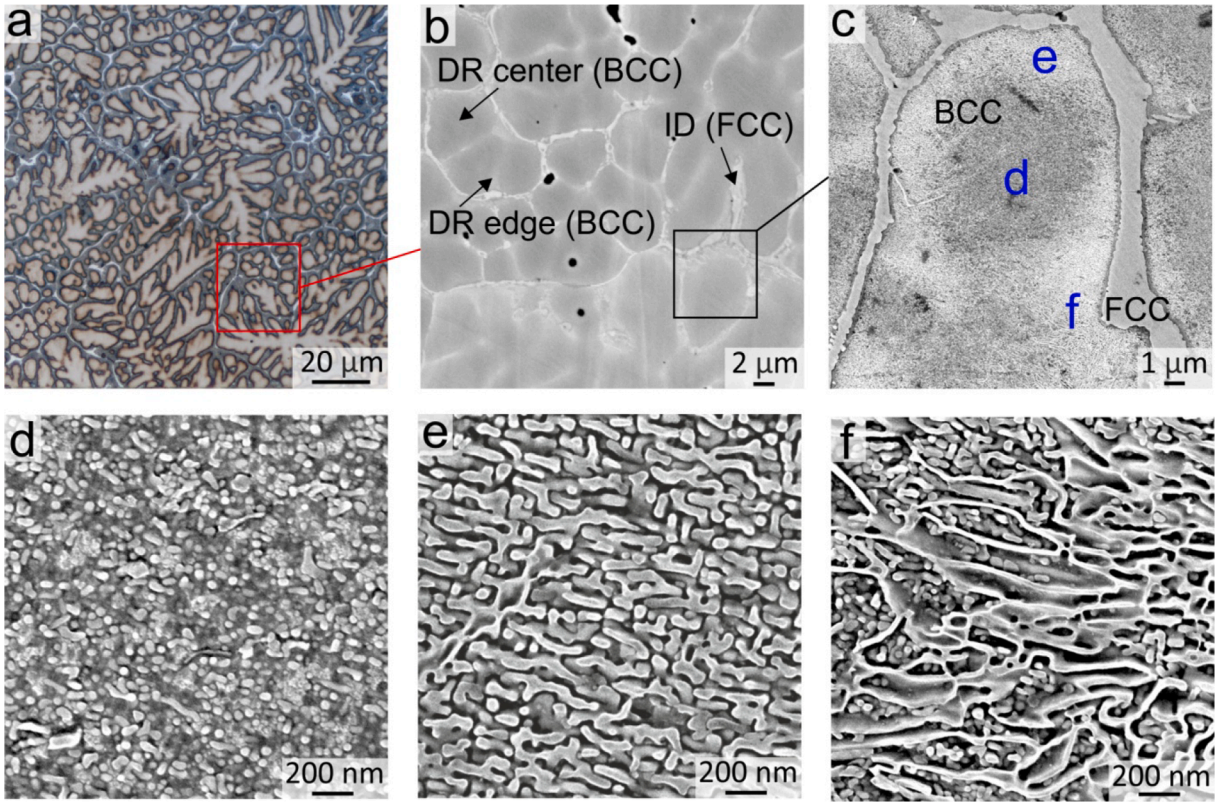

Fig. 4. Structure of the $AlCoCrFe_{0.6}Ni$ sample: (a) – LM; (b–f) – SEM, BSE mode, (c–f) – SEM SE mode, InLens Duo detector.

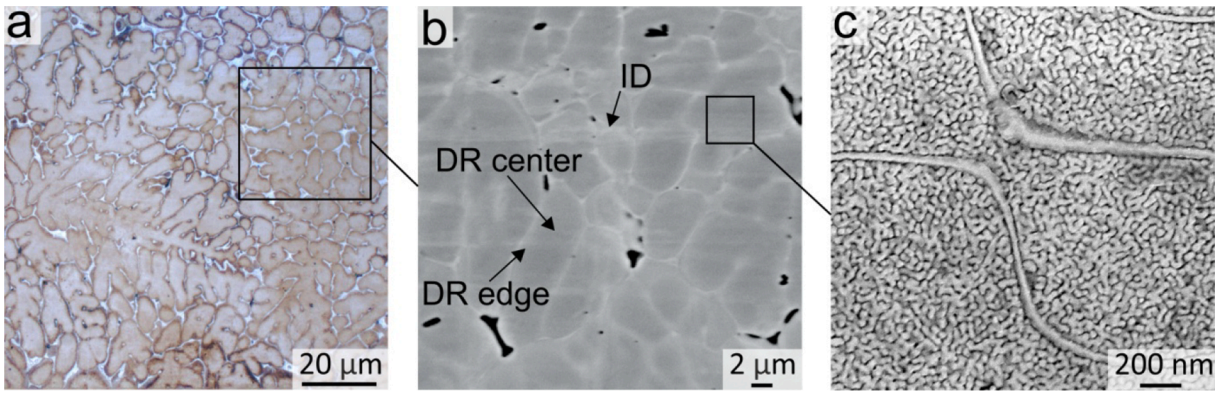

Fig. 5. Structure of the coating $Al_{1.5}CoCrFe_{0.5}Ni$: (a) LM; (b and c) SEM. The arrows in (b) indicate the areas of local EDX analysis (see results in Table 4).

mixture was formed in the shape of a nanosized wavy rippled texture with precipitations ~30 nm thick. In addition, long ribbon precipitates around 50 nm in thickness were observed throughout the nanosized wavy structure. Unlike the $AlCoCrFe_{0.6}Ni$ sample, the morphologies of the A2 + B2 mixture in the $Al_{1.5}CoCrFe_{0.5}Ni$ sample appeared similar both in the center and at the periphery of the dendrites, probably due to less pronounced element liquation and a more uniform distribution of Al.

The fcc-based $Al_{0.5}CoCrFe_{3.2}Ni$ sample predominantly consisted of elongated grains with cellular crystals inside (Fig. 6). Most cellular crystals grew in the direction perpendicular to the surface of the substrate. The formation of a distinct structure in the $Al_{0.5}CoCrFe_{3.2}Ni$ sample can be attributed to its narrower crystallization temperature range, as opposed to the two previously discussed samples.

The structure at the coating-substrate boundary differed from that of the main part of the sample due to the higher concentration of Fe near the substrate. In the $AlCoCrFe_{0.6}Ni$ sample, a 40 μm thick layer consisting of fcc crystals was found between the substrate and the coating. This layer contained a large amount of Fe (65–85 at. %). This indicates that for such a composition, the fcc phase was more favorable. As moving from the substrate towards the coating, the concentration of Fe and the tendency of the alloy to form the fcc phase decreased, and the fcc phase was formed only as a thin layer between large bcc grains (Fig. 7a). In the $Al_{1.5}CoCrFe_{0.5}Ni$ sample, an fcc interlayer was also formed at the coating-substrate boundary, but the average element composition of the sample didn't favor the formation of the fcc phase. Therefore, the expansion of fcc grains did not extend into the main part of the coating, stopping near the interface (Fig. 7b). In the fcc $Al_{0.5}CoCrFe_{3.2}Ni$ sample, a needle-shaped martensitic layer approximately 60 μm thick was formed near the coating-substrate boundary due to the local quenching of the alloy near the substrate (Fig. 7c inset).

Below the coating-substrate interface, a heat-affected zone was formed in the substrate of all three samples. The typical structure of the heat-affected zone formed near the coating-substrate interface in the low-carbon steel substrate during non-vacuum electron beam cladding of HEAs and intermetallic compounds was examined in detail in our previous studies [6,23].

3.1.4. EBSD analysis

The results of the EBSD analysis of the $Al_{0.5}CoCrFe_{3.2}Ni$ sample are shown in Fig. 8. While the grains near the substrate of the cladded layer didn't have a predominant crystallographic orientation, in the middle and upper parts of the coating, large grains 80 μm in width elongated in a ⟨1 0 0⟩ direction grew perpendicular to the substrate. Probably, during the initial stages of crystallization, the nucleation of randomly oriented grains occurred. As the crystallization front moved forward from the substrate toward the top surface, those crystals grew faster, whose growth direction ⟨1 0 0⟩ coincided with the direction of the fastest heat transfer. Such a ⟨1 0 0⟩ texture is typical for the directional crystallization of fcc and bcc alloys. Simultaneously with this process, grain growth with an "unfavorable" crystallographic orientation slowed down and stopped. Furthermore, a thin layer of equiaxed grains was observed on the top part of the coating. Most likely, this layer appeared due to heat transfer by convection and radiation during cooling of the surface layers of the coating.

The $AlCoCrFe_{0.6}Ni$ and $Al_{1.5}CoCrFe_{0.5}Ni$ samples (Fig. 9a and b)

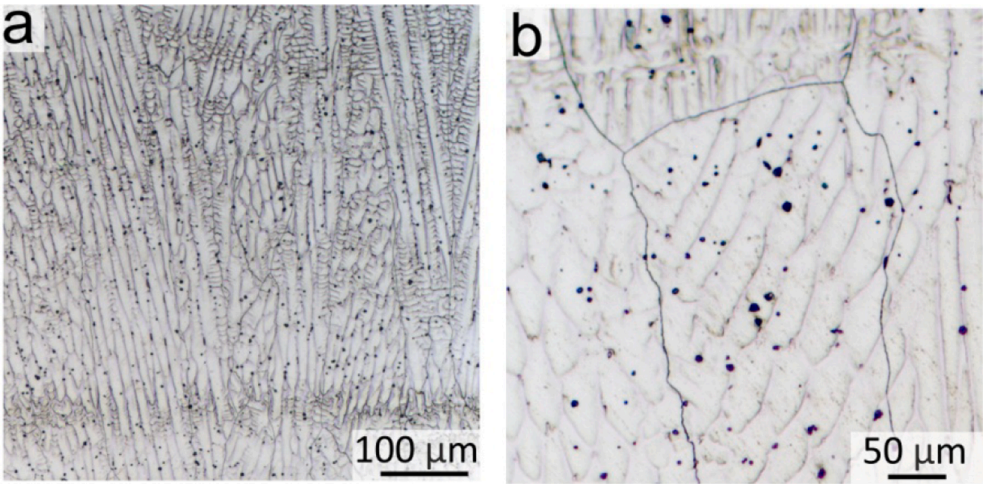

Fig. 6. Structure of the $Al_{0.5}CoCrFe_{3.2}Ni$ coating (LM).

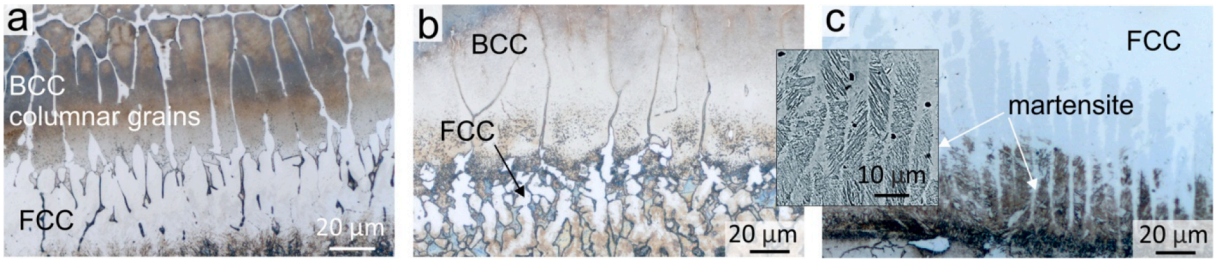

Fig. 7. Microstructure near the coating-substrate interface of $AlCoCrFe_{0.6}Ni$ (a), $Al_{1.5}CoCrFe_{0.5}Ni$ (b) and $Al_{0.5}CoCrFe_{3.2}Ni$ (c) samples (inset shows the needle-like structure observed by SEM).

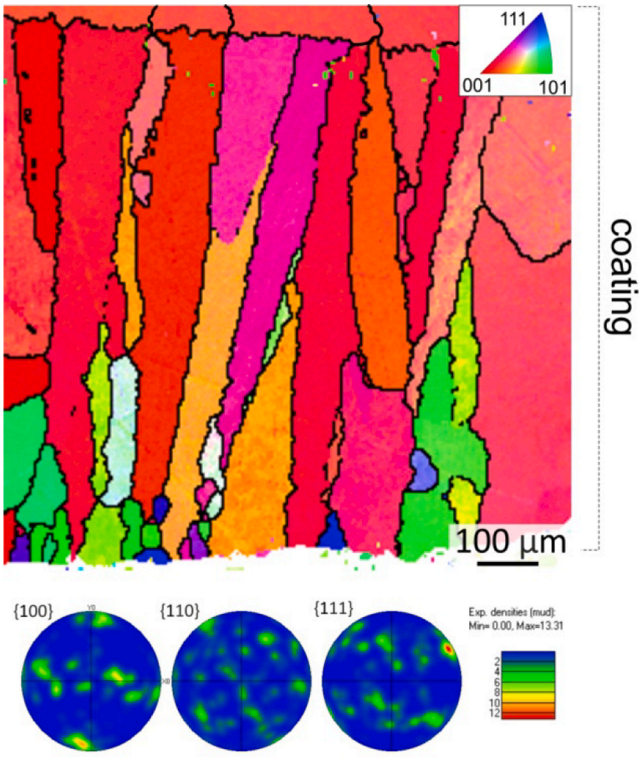

Fig. 8. IPF-map and pole figures of the $Al_{0.5}CoCrFe_{3.2}Ni$ sample.

predominantly consisted of the bcc phase with grain morphology different from that of the $Al_{0.5}CoCrFe_{3.2}Ni$ sample. Columnar grains with ⟨100⟩ direction perpendicular to the substrate were formed in the lower part of the coating, but in the middle and upper parts of the coating, equiaxed grains of ~65 μm in size were observed. In addition, the phase distribution maps (Fig. 9c and d) confirmed that the interlayer in the coating-surface interface in the samples $AlCoCrFe_{0.6}Ni$ and $Al_{1.5}CoCrFe_{0.5}Ni$, previously discovered in metallographic images, and thin films between the dendritic grains in the $AlCoCrFe_{0.6}Ni$ sample had an fcc structure.

The significant difference in the grain structure and texture of the bcc- and fcc-based coatings is most probably associated with differences in the crystallization temperatures, which were observed by SXRD analysis (see above Section 3.1.2. "SXRD analysis of coatings during heating"). The elongated grains observed throughout the entire $Al_{0.5}CoCrFe_{3.2}Ni$ coating and in the bottom part of $AlCoCrFe_{0.6}Ni$ and $Al_{1.5}CoCrFe_{0.5}Ni$ ones were formed when the crystallization front sequentially propagated from the substrate toward the top of the sample. In the upper and middle zones of the $AlCoCrFe_{0.6}Ni$ and $Al_{1.5}CoCrFe_{0.5}Ni$ coatings, equiaxed crystallographically disoriented grains appeared as a result of the emergence of a second crystallization front originating from the top of the samples, caused by convection and radiation transfer of heat. This suggests that the crystallization of bcc grains in the upper zones began at higher temperatures until these zones were reached by the crystallization front moving from the substrate. These conclusions are in agreement with the in-situ SXRD studies and literature data, which indicate that with an increase in Fe content in the bcc AlCoCrNi-Fe_x alloys, their crystallization temperature decreases [39,46].

Note that the thicknesses of the layers with equiaxed and elongated grains in the $AlCoCrFe_{0.6}Ni$ and $Al_{1.5}CoCrFe_{0.5}Ni$ samples were different. The average thickness of the layer with elongated grains in the $AlCoCrFe_{0.6}Ni$ sample (~275 μm) was larger than that in $Al_{1.5}CoCrFe_{0.5}Ni$ (~175 μm). This feature was also associated with the difference in the crystallization temperatures of the $AlCoCrFe_{0.6}Ni$ and $Al_{1.5}CoCrFe_{0.5}Ni$ coatings. In the lower part of the coatings, the alloy had a Fe-based composition (60–85 at. % of Fe), and the content of the other elements was not large. Thus, the crystallization temperatures and

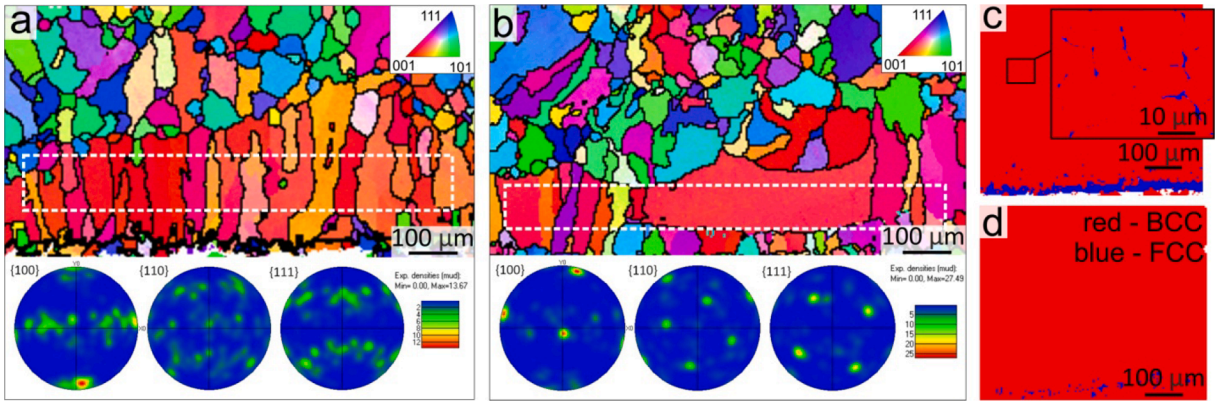

Fig. 9. IPF-maps and pole figures of the $AlCoCrFe_{0.6}Ni$ (a) and $Al_{1.5}CoCrFe_{0.5}Ni$ samples (b). (c) and (d) Show phase distribution maps corresponding to the IPF-maps in (a) and (b), respectively. The areas, which were used to plot the pole figures, are marked with dotted lines.

growth rates of the columnar grains in both samples were approximately the same. However, according to the in-situ SXRD data, the melting point of the main part of the coating $AlCoCrFe_{0.6}Ni$ was lower than that of the $Al_{1.5}CoCrFe_{0.5}Ni$ one. Accordingly, the equiaxed grains in the $AlCoCrFe_{0.6}Ni$ coating began to crystallize later upon cooling compared with those in $Al_{1.5}CoCrFe_{0.5}Ni$. Therefore, before the collision of the two crystallization fronts occurred, the columnar textured grains in the $AlCoCrFe_{0.6}Ni$ coating had time to grow deeper into the coating than those in the $Al_{1.5}CoCrFe_{0.5}Ni$ sample.

3.2. Mechanical properties of the samples

3.2.1. Microhardness

The bcc-based $Al_{1.5}CoCrFe_{0.5}Ni$ sample exhibited the highest microhardness (637 HV) (Fig. 10a). This can be attributed to the increased Al content and the high tendency to form an ordered B2 structure, which is known for its superior hardness compared with the disordered A2 structure. The hardness of the $AlCoCrFe_{0.6}Ni$ sample was slightly lower (563 HV), which is explained by its lower Al content compared with that of $Al_{1.5}CoCrFe_{0.5}Ni$ (Fig. 10b). Moreover, the $AlCoCrFe_{0.6}Ni$ coating contains a certain amount of the fcc phase. As a rule, the fcc phase in the Al-Co-Cr-Fe-Ni HEAs is more ductile than the bcc phase and has a lower hardness [57]. Consequently, the presence of fcc inclusions could reduce the overall microhardness of the sample. The fcc layers at the coating-substrate interface of $AlCoCrFe_{0.6}Ni$ and $Al_{1.5}CoCrFe_{0.5}Ni$ samples had lower hardness. This resulted in a gradual decrease in hardness in the coating-substrate transition zone, as can be seen in Fig. 10a and b. The microhardness of the fcc $Al_{0.5}CoCrFe_{3.2}Ni$ coating was 186 HV (Fig. 10c). However, at the coating-substrate boundary, a sharp increase in microhardness associated with the formation of a hard martensitic layer was observed. The underlying mechanism of the martensite formation can be explained as follows. As it was mentioned before, the amount of Fe near the boundary between the coating and the substrate greatly increases and reaches 85 at. %. In fact, in this area, the composition of the coating corresponds to a composition of alloyed steel, which in stable condition should have bcc structure. Due to the high cooling rates typical for electron beam cladding, the martensite forms near the substrate of the $Al_{0.5}CoCrFe_{3.2}Ni$ sample at the cooling stage.

3.2.2. Dry sliding wear behavior

The results of the dry sliding wear tests are presented in Fig. 11. Note, that the wear behavior of the coatings on a substrate can be estimated by a lot of contact models, which take into account the gradient layers and finite thicknesses of the coatings [58–61]. Considering the wear tests in the present study, it should be taken into account that the coatings described in the manuscript have a thickness ranging from 600 to 900 μm. The average depth of the wear dimples on $Al_{0.5}CoCrFe_{3.2}Ni$ and $AlCoCrFe_{0.6}Ni$ samples was ~60 μm (Fig. 12 a, b), and ~38 μm on the $Al_{1.5}CoCrFe_{0.5}Ni$ sample (Fig. 12c). The most parts of all the obtained coatings are homogeneous and have the structures shown in Figs. 4a, 5a, and 6a, respectively. The transition zones with different structure near

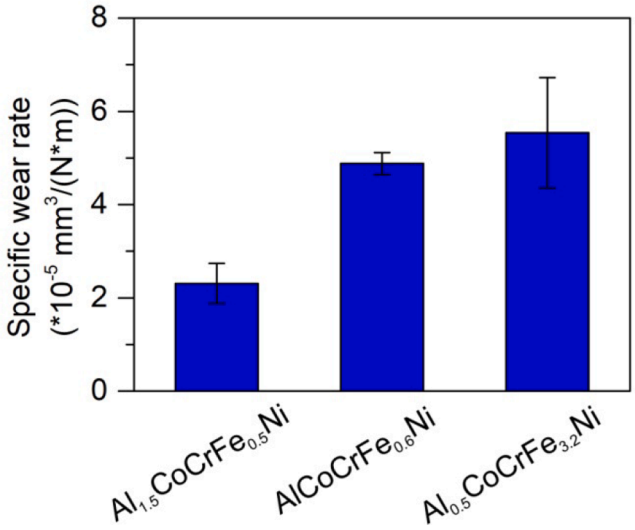

Fig. 11. Specific wear rate of the HEA coatings during dry sliding wear tests.

the substrate didn't exceed 100 μm in thickness (see gradient zones in Fig. 7). Thus, wear conditions in this case can be considered as wear tests of bulk materials.

$Al_{1.5}CoCrFe_{0.5}Ni$ sample showed the highest wear resistance under dry sliding wear conditions with a specific wear rate of 2.30×10^{-5} $mm^3/(N \times m)$. The high result exhibited by this sample is related to the good resistance of the hard B2 bcc phase to plastic deformation and delamination, which allows the coating to withstand abrasion [29,39,62]. In many cases, the wear resistance of a material is directly related to its hardness. Even though the average microhardness of $Al_{1.5}CoCrFe_{0.5}Ni$ and $AlCoCrFe_{0.6}Ni$ samples was approximately the same, the latter showed twice lower resistance to wear.

After the wear test, the cross-sectional structure of $AlCoCrFe_{0.6}Ni$ sample differed significantly from that of $Al_{0.5}CoCrFe_{3.2}Ni$ and $Al_{1.5}CoCrFe_{0.5}Ni$ ones. In the $Al_{0.5}CoCrFe_{3.2}Ni$ and $Al_{1.5}CoCrFe_{0.5}Ni$ samples, thin deformed layers of the initial structure were observed (Fig. 13a and b, respectively). Due to greater ductility, the thickness of the deformed layer in the $Al_{0.5}CoCrFe_{3.2}Ni$ sample is larger (~54 μm, compared to $Al_{1.5}CoCrFe_{0.5}Ni$ one, which is ~16 μm), and the plastic strain is greater, as can be seen from the shape of deformed cellular crystals. In the $AlCoCrFe_{0.6}Ni$ sample, the mechanically mixed layer (MML) was found on the top of the wear surface; it had a different structure compared to the initial structure of the sample. The thickness of MML varied from 10 to 60 μm. EDX analysis revealed that the composition of MML matched the average composition of the coating; no presence of oxygen or tungsten from the counterbody was detected. The cracks in this layer (Fig. 13c and d, shown with an arrow) evidenced that the structure hardened and embrittled during its formation. Presumably, MML partly delaminated and moved out from the wear dimple during tests, and promoted higher wear rates. The delamination of

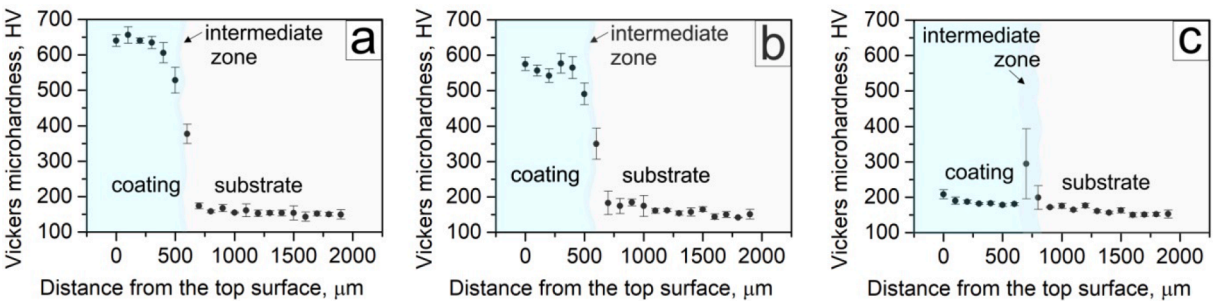

Fig. 10. Microhardness of coatings produced by non-vacuum electron beam cladding (a) – $Al_{1.5}CoCrFe_{0.5}Ni$, (b) – $AlCoCrFe_{0.6}Ni$, and (c) – $Al_{0.5}CoCrFe_{3.2}Ni$.

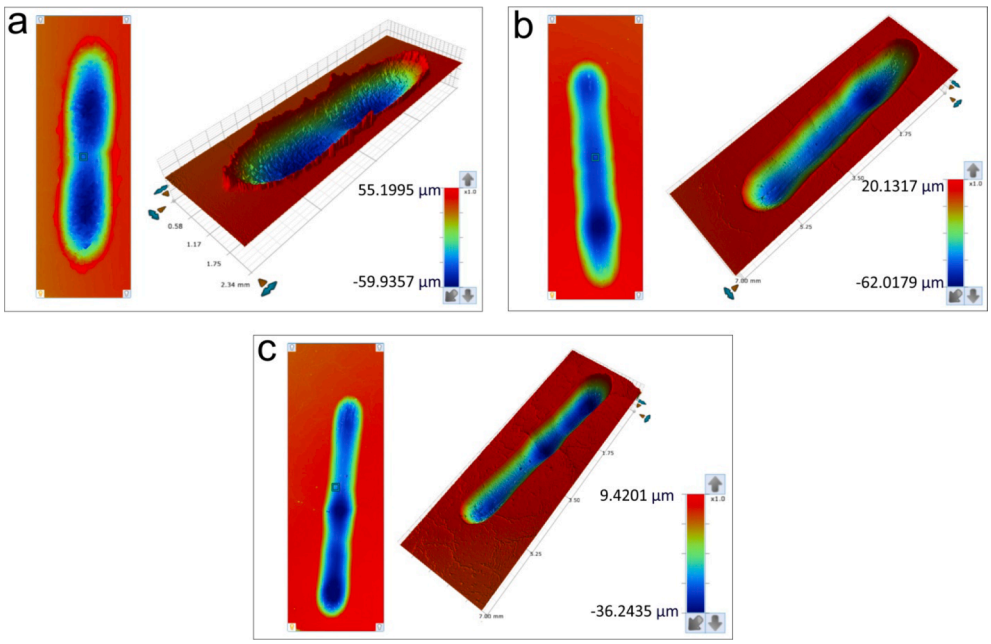

Fig. 12. Reliefs of the wear dimples after dry sliding wear tests, recorded using an optical profilometer (a) $Al_{0.5}CoCrFe_{3.2}Ni$ sample, (b) $AlCoCrFe_{0.6}Ni$ sample, and (c) $Al_{1.5}CoCrFe_{0.5}Ni$ sample.

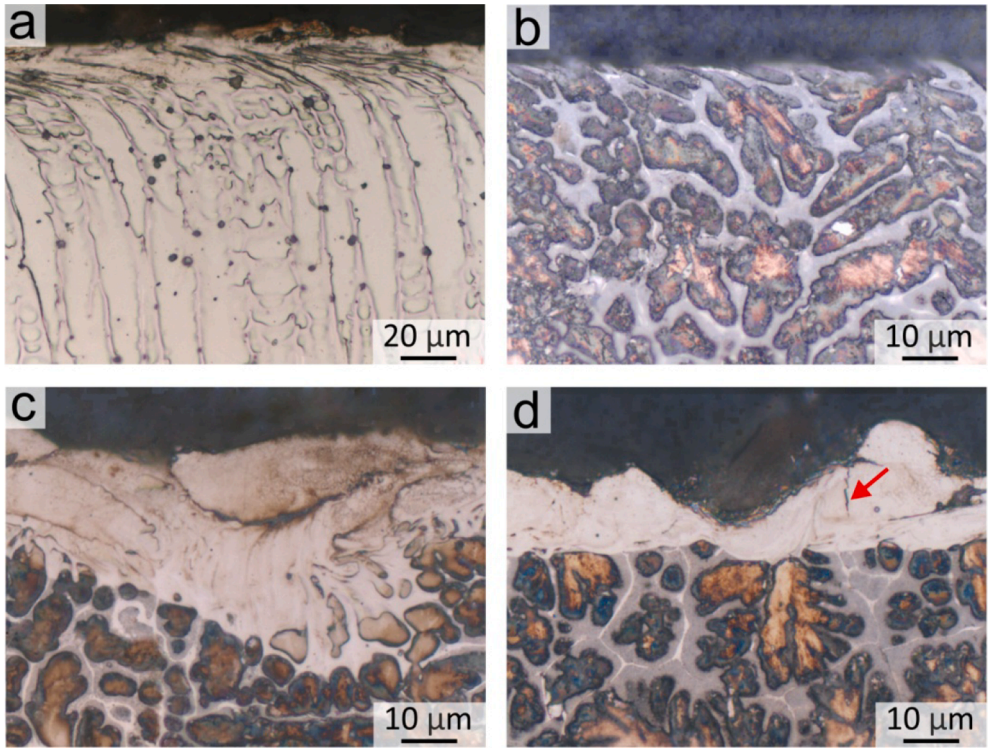

Fig. 13. Cross-section of the wear dimple after dry sliding wear tests (a) $Al_{0.5}CoCrFe_{3.2}Ni$ sample, (b) $Al_{1.5}CoCrFe_{0.5}Ni$ sample, (c and d) $AlCoCrFe_{0.6}Ni$ sample (OM).

brittle MML and the corresponding increase in mass loss during dry sliding wear of HEAs were also described in [63].

The $Al_{0.5}CoCrFe_{3.2}Ni$ sample consisted of only a ductile fcc phase, thus, it showed the highest specific wear rate of 5.54×10^{-5} $mm^3/(N \times m)$. However, although the microhardness of the $Al_{0.5}CoCrFe_{3.2}Ni$ sample was 3 times less than that of $AlCoCrFe_{0.6}Ni$, their specific wear rates were very similar. This was related to the special wear behavior of the fcc-based HEAs. The topography of the samples after the tests revealed the formation of a bead with a height of about 25 µm at the edges of the wear dimple (Fig. 12a). This suggests that the fcc coatings experienced noticeable plastic deformation due to sliding wear. At the same time, the bcc coatings exhibited smooth and even crater edges, with no evidence of material displacement on a significant scale (Fig. 12b). A lot of fcc Fe-based alloys [64] and fcc HEAs [29,33,65,66] undergo work hardening during friction. For this reason, despite their low microhardness, they can exhibit good wear resistance. Therefore, the $Al_{0.5}CoCrFe_{3.2}Ni$ sample, which predominantly consisted of fcc phase, exhibited a wear rate comparable to that of $AlCoCrFe_{0.6}Ni$, which

consisted of bcc A2 + B2 phase.

Thus, under some operating conditions, the use of Fe-rich fcc AlCoCrFeNi alloys may be more cost-effective. This can happen, for example, in situations where both wear resistance and a high level of reliability and crack resistance are required, which can't be provided by hard but more brittle B2 bcc-based AlCoCrFeNi alloys.

SEM images of the wear surface, typical for coatings with a predominance of the bcc phase ($AlCoCrFe_{0.6}Ni$ and $Al_{1.5}CoCrFe_{0.5}Ni$ samples), are shown in Fig. 14. These samples demonstrated a smooth wear surface with shallow grooved scratches from wear debris (indicated by arrows in Fig. 14a and b), which indicates the predominance of the abrasive wear mechanism. In some local areas, the counterbody flattened and imprinted wear debris into the surface of the sample. EDX analysis of such inclusions revealed the presence of elements of the coating and a large amount of oxygen. Apparently, during sliding, the mechanically activated wear debris reacted with the oxygen in the air, resulting in the formation of oxides of the coating elements. Scratches were also revealed on the imprinted wear debris (Fig. 14c–f). Mild oxidation and adhesion wear of Al-Co-Cr-Fe-Ni HEAs during sliding friction at room temperature were also observed in [29,39,62].

SEM analysis of the wear surface of the $Al_{0.5}CoCrFe_{3.2}Ni$ fcc sample revealed the formation of ploughing grooves, as shown in Fig. 15a and b. Due to the higher ductility of the fcc phase, many debris particles weren't carried out from the wear dimple but stuck and adhered to the wear surface. They were actively mixed by the counterbody with the material of the sample and partially penetrated into the sample surface (Fig. 15d). In some places, the oxidized layers, which adhered to the wear surface, exfoliated and formed a rougher wear surface morphology (Fig. 15a, c, e, f). Meghwal et al. [62] also observed that during the dry sliding wear of AlCoCrFeNi HEA, some of the debris were converted to oxides due to frictional heat, pierced through the soft fcc phase, and acted as a barrier, reducing mass loss. Thus, in some cases, the oxidation wear mechanism can also have a beneficial effect on the wear resistance of HEAs.

4. Conclusions

1) Al-Co-Cr-Fe-Ni HEA coatings with different amounts of Al in powder mixtures were obtained by non-vacuum electron beam cladding. It was revealed that with the change of the Al molar ratio in the powder mixture from 0.5 to 1.5, the content of Fe, which enters the coating from the steel substrate, changed from 9.9 at. % up to 48.1 at. %. The average stoichiometric compositions of the samples after the cladding were $Al_{0.5}CoCrFe_{3.2}Ni$, $AlCoCrFe_{0.6}Ni$, and $Al_{1.5}CoCrFe_{0.5}Ni$; they consisted of fcc, bcc + fcc, and bcc phases, respectively.
2) In-situ SXRD analysis showed that the $Al_{0.5}CoCrFe_{3.2}Ni$ sample had the lowest solidus temperature of approximately 1200 °C, and the $Al_{1.5}CoCrFe_{0.5}Ni$ sample had a relatively high solidus temperature of around 1425 °C with a liquidus temperature above 1500 °C. As a result, the crystallization of the $Al_{1.5}CoCrFe_{0.5}Ni$ sample after cladding began at higher temperatures. The brief period in the liquid state meant that only 9.9 at. % of Fe entered the sample from the substrate. Conversely, the lower solidus temperature of the $Al_{0.5}CoCrFe_{3.2}Ni$ sample resulted in a longer duration in the liquid

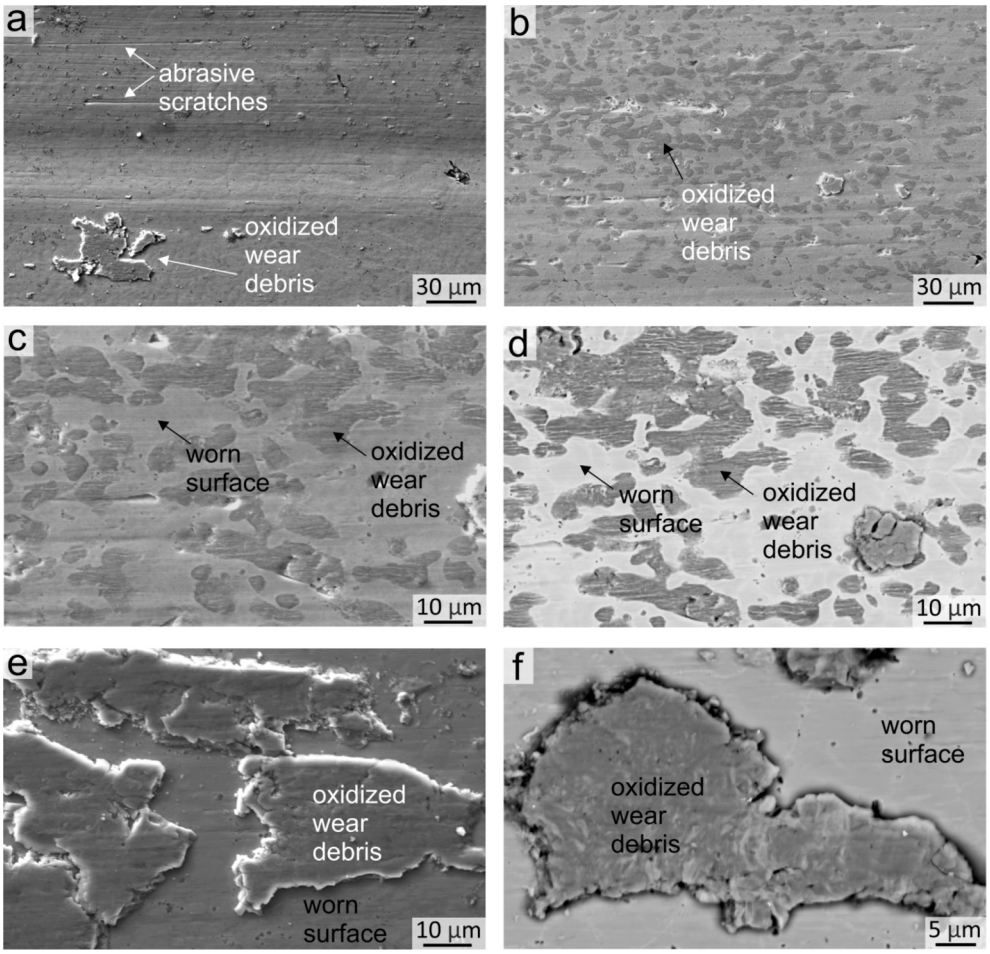

Fig. 14. Typical morphology of the wear surface of the $AlCoCrFe_{0.6}Ni$ and $Al_{1.5}CoCrFe_{0.5}Ni$ samples after dry sliding wear tests; (a and b) general view, (c and d) oxidized wear debris flattened out and imprinted on the wear surface of the $AlCoCrFe_{0.6}N$ sample, (e and f) large oxidized debris flattened on the wear surface of the $AlCoCrFe_{0.6}N$ sample. (a–c, e) SEM secondary electron detector (d and f) SEM backscatter electron detector.

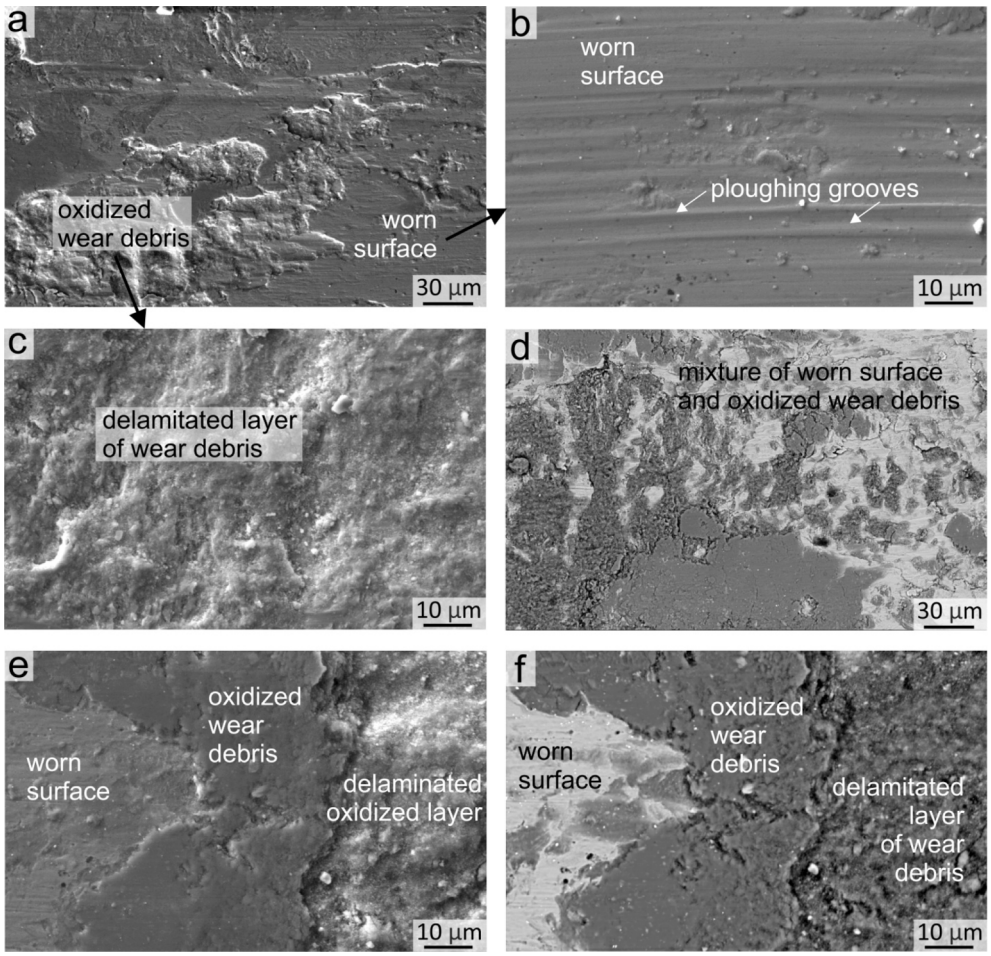

Fig. 15. The wear surface of the $Al_{0.5}CoCrFe_{3.2}Ni$ sample after dry sliding wear tests; (a) low magnification view, (b) ploughing grooves on the wear surface, (c) oxidized and exfoliated debris on the wear surface, (d) SEM backscatter electron detector image of the mixed structure of the wear surface and oxidized wear debris, (e) three zones with wear surface, oxidized flattened and delaminated oxidized wear debris, (f) SEM backscatter electron image of the figure (e).

state, allowing for a higher incorporation of Fe from the substrate (48.1 at.%) into the coating.

3) In the $Al_{0.5}CoCrFe_{3.2}Ni$ sample, the crystallization front propagated from the substrate into the coating and promoted the formation of columnar grains with a ⟨1 0 0⟩ direction perpendicular to the substrate. Because of the higher solidus temperatures of the $AlCoCrFe_{0.6}Ni$ and $Al_{1.5}CoCrFe_{0.5}Ni$ samples, their crystallization began both from the top and bottom parts of the coatings. This contributed to the formation of equiaxed grains in the main part of the coatings.
4) The $Al_{1.5}CoCrFe_{0.5}Ni$ bcc sample exhibited the highest microhardness of 637 HV and wear resistance during dry sliding friction. On the other hand, the fcc $Al_{0.5}CoCrFe_{3.2}Ni$ sample had a low microhardness of 186 HV, but due to the work hardening, it demonstrated a comparable specific wear rate to that of the bcc + fcc $AlCoCrFe_{0.6}Ni$ sample, which had a hardness of 563 HV.
5) Al-rich AlCoCrFeNi coatings can be recommended for application in wear operating conditions. Cost-effective Fe-rich AlCoCrFeNi coatings can be used in critical structure units, when satisfactory wear resistance, high reliability, and crack resistance are required. By varying the parameters of non-vacuum electron beam cladding, one can control the amount of Fe in the coatings. From the results obtained, it follows that when cladding Ni-rich AlCoCrFeNi powder mixtures, a lower energy density is required to receive coatings with the same Fe content as in the Al-rich ones.

CRediT authorship contribution statement

T.S. Ogneva: Writing – original draft, Supervision, Project administration, Methodology, Investigation, Formal analysis, Data curation, Conceptualization. **K.I. Emurlaev:** Writing – review & editing, Visualization, Software, Methodology, Investigation. **K.E. Kuper:** Software, Resources, Methodology, Investigation. **N. Malyutina Yu:** Methodology, Investigation. **E.V. Domarov:** Resources, Methodology, Investigation. **I.K. Chakin:** Resources, Methodology, Investigation. **K.A. Skorokhod:** Methodology, Investigation. **A.A. Ruktuev:** Writing – review & editing, Methodology, Investigation. **I.E. Nasennik:** Investigation, Methodology. **I.A. Bataev:** Writing – review & editing, Writing – original draft, Supervision, Software, Resources, Methodology, Investigation.

Declaration of competing interest

The authors declare that they have no known competing financial interests or personal relationships that could have appeared to influence the work reported in this paper.

Data availability

Data will be made available on request.

Acknowledgements

The study was supported by the Ministry of Science and Higher Education of the Russian Federation as a part of the state task FSUN-2024-0005 “Structural transformations in surface layers of metal alloys under extreme thermal and deformation impacts”.

The microstructure of the samples was analyzed at core facility center “Structure, mechanical and physical properties of materials”, NSTU.

The synchrotron X-ray diffraction analysis was carried out at “Siberian Synchrotron and Terahertz Radiation Centre”.

Wear tests were carried out using the equipment of the Equipment Sharing Center “Mechanics” of ITAM SB RAS.

References

[1] J. Yeh, S. Chen, S. Lin, J. Gan, T. Chin, T. Shun, C. Tsau, S. Chang, Nanostructured high-entropy alloys with multiple principal elements: novel alloy design concepts and outcomes, Adv. Eng. Mater. 6 (2004) 299–303.

[2] R. Chen, T. Xie, B. Wu, L. Weng, H. Ali, S. Yang, Y. Zhao, P. Zhao, C. Zhang, R. Cao, J. Wen, Q. Yao, Q. Cai, H. Zhang, B. Sa, C. Wen, M. Lin, X. Sun, H. Su, Y. Liu, C. Wang, A general approach to simulate the atom distribution, lattice distortion, and mechanical properties of multi-principal element alloys based on site preference: Using FCC_CoNiV and CoCrNi to demonstrate and compare, J. Alloys Compd. 935 (2023) 168016, https://doi.org/10.1016/j.jallcom.2022.168016.

[3] K. Chen, Z. Xiong, M. An, X. Cheng, Effect of Fe content on microstructures and mechanical properties of eutectic Co-Cr-Fe-Ni-Hf multi-principal element alloys, J. Alloys Compd. 939 (2023) 168724, https://doi.org/10.1016/j.jallcom.2023.168724.

[4] P. Sreeramagiri, P. Sharma, C. Das, G. Balasubramanian, Examining solid-state sintering of AlCoCrFeNi multi-principal element alloy by molecular simulations, Comput. Mater. Sci. 216 (2023) 111875, https://doi.org/10.1016/j.commatsci.2022.111875.

[5] Z.B. Bataeva, A.A. Ruktuev, I.V. Ivanov, A.B. Yurgin, I.A. Bataev, Review of alloys developed using the entropy approach, Obrab. Met. (tekhnologiya, Oborudovanie, Instrumenty) = Met. Work. Mater. Sci. 23 (2021) 116–146, https://doi.org/10.17212/1994-6309-2021-23.2-116-146.

[6] A.A. Ruktuev, D.V. Lazurenko, T.S. Ogneva, R.I. Kuzmin, M.G. Golkovski, I. A. Bataev, Structure and oxidation behavior of CoCrFeNiX (where X is Al, Cu, or Mn) coatings obtained by electron beam cladding in air atmosphere, Surf. Coat. Technol. 448 (2022) 128921, https://doi.org/10.1016/j.surfcoat.2022.128921.

[7] N. Birbilis, S. Choudhary, J.R. Scully, M.L. Taheri, A perspective on corrosion of multi-principal element alloys, NPJ Mater. Degrad. 5 (2021) 14, https://doi.org/10.1038/s41529-021-00163-8.

[8] A. Silvello, E. Torres Diaz, E. Rúa Ramirez, I. Garcia Cano, Microstructural, mechanical and wear properties of atmospheric plasma-sprayed and high-velocity oxy-fuel AlCoCrFeNi equiatomic high-entropy alloys (HEAs) coatings, J. Therm. Spray Technol. (2023), https://doi.org/10.1007/s11666-022-01520-y.

[9] Y. Shi, B. Yang, P.K. Liaw, Corrosion-resistant high-entropy alloys: a review, Metals (Basel) 7 (2017) 43.

[10] F. Zhang, L. Wang, S. Yan, G. Yu, J. Chen, F. Yin, High temperature oxidation behavior of atmosphere plasma sprayed AlCoCrFeNi high-entropy alloy coatings, Mater. Chem. Phys. 282 (2022) 125939, https://doi.org/10.1016/j.matchemphys.2022.125939.

[11] Q. Liu, T. Dong, B. Fu, G. Li, L. Yang, Effect of laser remelting on microstructure and properties of AlCoCrFeNi high-entropy alloy coating, J. Mater. Eng. Perform. 30 (2021) 5728–5735, https://doi.org/10.1007/s11665-021-05806-0.

[12] D.G. Shaysultanov, N.D. Stepanov, A.V. Kuznetsov, G.A. Salishchev, O.N. Senkov, Phase composition and superplastic behavior of a wrought AlCoCrCuFeNi high-entropy alloy, JOM 65 (2013) 1815–1828, https://doi.org/10.1007/s11837-013-0754-5.

[13] H. Liu, Q. Gao, J. Dai, P. Chen, W. Gao, J. Hao, H. Yang, Microstructure and high-temperature wear behavior of CoCrFeNiWx high-entropy alloy coatings fabricated by laser cladding, Tribol. Int. 172 (2022) 107574, https://doi.org/10.1016/j.triboint.2022.107574.

[14] H. Liu, R. Wang, Q. Wang, P. Chen, H. Yang, J. Hao, S. Sun, X. Liu, Tribology behavior in laser cladded dual-phase AlxCoCrFeNiMn(1–x) high entropy alloys influenced by hierarchical interface architecture, Surf. Coatings Technol. 471 (2023) 129895, https://doi.org/10.1016/j.surfcoat.2023.129895.

[15] A. Sharma, High entropy alloy coatings and technology, Coatings 11 (2021) 372.

[16] L. Wang, F. Zhang, S. Yan, G. Yu, J. Chen, J. He, F. Yin, Microstructure evolution and mechanical properties of atmosphere plasma sprayed AlCoCrFeNi high-entropy alloy coatings under post-annealing, J. Alloys Compd. 872 (2021) 159607, https://doi.org/10.1016/j.jallcom.2021.159607.

[17] Q. Fan, C. Chen, C. Fan, Z. Liu, X. Cai, S. Lin, C. Yang, AlCoCrFeNi high-entropy alloy coatings prepared by gas tungsten arc cladding: microstructure, mechanical and corrosion properties, Intermetallics 138 (2021) 107337, https://doi.org/10.1016/j.intermet.2021.107337.

[18] Q. Fan, C. Chen, C. Fan, Z. Liu, X. Cai, S. Lin, C. Yang, Effect of high Fe content on the microstructure, mechanical and corrosion properties of AlCoCrFeNi high-entropy alloy coatings prepared by gas tungsten arc cladding, Surf. Coat. Technol. 418 (2021) 127242, https://doi.org/10.1016/j.surfcoat.2021.127242.

[19] A. Anupam, R.S. Kottada, S. Kashyap, A. Meghwal, B.S. Murty, C.C. Berndt, A.S. M. Ang, Understanding the microstructural evolution of high entropy alloy coatings manufactured by atmospheric plasma spray processing, Appl. Surf. Sci. 505 (2020) 144117, https://doi.org/10.1016/j.apsusc.2019.144117.

[20] H. Guan, L. Chai, Y. Wang, K. Xiang, L. Wu, H. Pan, M. Yang, C. Teng, W. Zhang, Microstructure and hardness of NbTiZr and NbTaTiZr refractory medium-entropy alloy coatings on Zr alloy by laser cladding, Appl. Surf. Sci. 549 (2021) 149338, https://doi.org/10.1016/j.apsusc.2021.149338.

[21] A.A. Ruktuev, M.G. Golkovski, D.V. Lazurenko, V.A. Bataev, I.V. Ivanov, A. Thömmes, I.A. Bataev, TiTaNb clads produced by electron beam surface alloying in regular air at atmospheric pressure: fabrication, structure, and properties, Mater. Charact. 179 (2021), https://doi.org/10.1016/j.matchar.2021.111375.

[22] T.A. Zimogliadova, A.A. Bataev, D. V. Lazurenko, I.A. Bataev, V.A. Bataev, M.G. Golkovskii, H. Saage, T.S. Ogneva, A.A. Ruktuev, Structural characterization of layers fabricated by non-vacuum electron beam cladding of Ni-Cr-Si-B self-fluxing alloy with additions of niobium and boron, Mater. Today Commun. 33 (2022) 104363. doi:10.110.1016/j.mtcomm.2022.104363.

[23] T.S. Ogneva, A.A. Ruktuev, D.V. Lazurenko, K.I. Emurlaev, Y.N. Malyutina, M. G. Golkovsky, K.D. Egoshin, I.A. Bataev, Structure and oxidation behavior of NiAl-based coatings produced by non-vacuum electron beam cladding on low-carbon steel, Metals (Basel) 12 (2022) 1679.

[24] K. Osintsev, S. Konovalov, Y. Ivanov, V. Gromov, S. Vorobyev, I. Panchenko, Characterization of Al-Co-Cr-Fe-Mn-Ni high-entropy alloy coating fabricated onto AA5083 using wire-arc additive manufacturing, Metals (Basel) 12 (2022), https://doi.org/10.3390/met12101612.

[25] K. Kuwabara, H. Shiratori, T. Fujieda, K. Yamanaka, Y. Koizumi, A. Chiba, Mechanical and corrosion properties of AlCoCrFeNi high-entropy alloy fabricated with selective electron beam melting, Addit. Manuf. 23 (2018) 264–271, https://doi.org/10.1016/j.addma.2018.06.006.

[26] V. Gromov, Y. Ivanov, S. Konovalov, K. Osintsev, A. Semin, Y. Rubannikova, Modification of high-entropy alloy AlCoCrFeNi by electron beam treatment, J. Mater. Res. Technol. 13 (2021) 787–797, https://doi.org/10.1016/j.jmrt.2021.05.012.

[27] T. Ogneva, K. Emurlaev, Y. Malyutina, E. Domarov, I. Chakin, A. Ruktuev, P. Riabinkina, A. Yurgin, I. Bataev, Heat treatment induced structural transformations and high-temperature oxidation behavior of Al21Co22Cr22Fe13Ni22 high-entropy coatings produced by non-vacuum electron beam cladding, Metals (Basel) 13 (2023), https://doi.org/10.3390/met13101689.

[28] H.R. Sistla, J.W. Newkirk, F. Frank Liou, Effect of Al/Ni ratio, heat treatment on phase transformations and microstructure of AlxFeCoCrNi2-x (x=0.3, 1) high entropy alloys, Mater. Des. 81 (2015) 113–121, https://doi.org/10.1016/j.matdes.2015.05.027.

[29] J. Joseph, N. Haghdadi, K. Shamlaye, P. Hodgson, M. Barnett, D. Fabijanic, The sliding wear behaviour of CoCrFeMnNi and AlxCoCrFeNi high entropy alloys at elevated temperatures, Wear 428–429 (2019) 32–44, https://doi.org/10.1016/j.wear.2019.03.002.

[30] M. Li, J. Gazquez, A. Borisevich, R. Mishra, K.M. Flores, Evaluation of microstructure and mechanical property variations in AlxCoCrFeNi high entropy alloys produced by a high-throughput laser deposition method, Intermetallics 95 (2018) 110–118, https://doi.org/10.1016/j.intermet.2018.01.021.

[31] M.M. Garlapati, M. Vaidya, A. Karati, S. Mishra, R. Bhattacharya, B.S. Murty, Influence of Al content on thermal stability of nanocrystalline AlxCoCrFeNi high entropy alloys at low and intermediate temperatures, Adv. Powder Technol. 31 (2020) 1985–1993, https://doi.org/10.1016/j.apt.2020.02.032.

[32] M. Fereidouni, M. Sarkari Khorrami, M. Heydarzadeh Sohi, Liquid phase cladding of AlxCoCrFeNi high entropy alloys on AISI 304L stainless steel, Surf. Coat. Technol. 402 (2020) 126331, https://doi.org/10.1016/j.surfcoat.2020.126331.

[33] J. Joseph, P. Hodgson, T. Jarvis, X. Wu, N. Stanford, D.M. Fabijanic, Effect of hot isostatic pressing on the microstructure and mechanical properties of additive manufactured AlxCoCrFeNi high entropy alloys, Mater. Sci. Eng. A 733 (2018) 59–70, https://doi.org/10.1016/j.msea.2018.07.036.

[34] M. Golkovsky, Hardening and Surfacing with a Beam of Relativistic Electrons, LAP LAMBERT Academic Publishing, 2013 [in Russian].

[35] H. Ren, R.R. Chen, X.F. Gao, T. Liu, G. Qin, S.P. Wu, J.J. Guo, High-performance AlCoCrFeNi high entropy alloy with marine application perspective, J. Mater. Res. Technol. 25 (2023) 6751–6763, https://doi.org/10.1016/j.jmrt.2023.07.135.

[36] S. Guo, C. Ng, J. Lu, C.T. Liu, Effect of valence electron concentration on stability of fcc or bcc phase in high entropy alloys, J. Appl. Phys. 109 (2011) 103505.

[37] F. Tian, L. Delczeg, N. Chen, L.K. Varga, J. Shen, L. Vitos, Structural stability of NiCoFeCrAl x high-entropy alloy from ab initio theory, Phys. Rev. B 88 (2013) 85128.

[38] J. Saha, P.V. Cobbinah, T. Hiroto, S. Matsunaga, Y. Toda, Y. Yamabe-Mitarai, Tailoring of the microstructure and texture of al-containing cocrni medium entropy alloys during severe warm-rolling, Available SSRN 4446907. (n.d.).

[39] G.J. Zhang, Q.W. Tian, K.X. Yin, S.Q. Niu, M.H. Wu, W.W. Wang, Y.N. Wang, J. C. Huang, Effect of Fe on microstructure and properties of AlCoCrFexNi (x=1.5, 2.5) high entropy alloy coatings prepared by laser cladding, Intermetallics 119 (2020) 106722, https://doi.org/10.1016/j.intermet.2020.106722.

[40] M. Ostrowska, P. Riani, B. Bocklund, Z.-K. Liu, G. Cacciamani, Thermodynamic modeling of the Al-Co-Cr-Fe-Ni high entropy alloys supported by key experiments, J. Alloys Compd. 897 (2022) 162722.

[41] P. Rogl, M. Materials Science International Team, Partial isothermal section at 1150°C after [85Ofo]: Datasheet from MSI Eureka in SpringerMaterials. Stuttgart

(1991). Accessed: 11-04-2024, (n.d.). https://materials.springer.com/msi/phase-diagram/docs/sm_msi_r_10_012731_01_full_LnkDia5.
[42] S.M. Hao, T. Takayama, K. Ishida, T. Nishizawa, Miscibility gap in Fe-Ni-Al and Fe-Ni-Al-Co systems, Metall. Trans. A 15 (1984) 1819–1828, https://doi.org/10.1007/BF02664895.
[43] M. Hubert-Protopopescu, H. Hubert, M. Materials Science International Team, Al-Co-Ni Ternary Phase Diagram Evaluation. Phase diagrams, crystallographic and thermodynamic data: Datasheet from MSI Eureka in SpringerMaterials, in: G. Effenberg (Ed.). Stuttgart (2014) Accessed: 11-04-2024, (n.d.). https://materials.springer.com/msi/docs/sm_msi_r_10_011478_01.
[44] P. Budberg and A. Prince, G. Cacciamani, R. Ferro, B. Grushko, P. Perrot, R. Schmid-Fetzer, M. Materials Science International Team, Al-Fe-Ni Ternary Phase Diagram Evaluation · Phase diagrams, crystallographic and thermodynamic data: Datasheet from MSI Eureka in SpringerMaterials. Stuttgart (2014). Accessed: 11-04-2024, (n.d.). https://materials.springer.com/msi/docs/sm_msi_r_10_010205_02.
[45] O. Stryzhyboroda, V.T. Witusiewicz, S. Gein, D. Röhrens, U. Hecht, Phase equilibria in the Al–Co–Cr–Fe–Ni high entropy alloy system: thermodynamic description and experimental study, Front. Mater. 7 (2020), https://doi.org/10.1016/j.jallcom.2022.168016.
[46] Y. Zhang, X. Yang, P.K. Liaw, Alloy design and properties optimization of high-entropy alloys, JOM 64 (2012) 830–838, https://doi.org/10.1007/s11837-012-0366-5.
[47] D. Karlsson, P. Beran, L. Riekehr, J.-C. Tseng, P. Harlin, U. Jansson, J. Cedervall, Structure and phase transformations in gas atomized AlCoCrFeNi high entropy alloy powders, J. Alloys Compd. 893 (2022) 162060, https://doi.org/10.1016/j.jallcom.2021.162060.
[48] E. Strumza, S. Hayun, Comprehensive study of phase transitions in equiatomic AlCoCrFeNi high-entropy alloy, J. Alloys Compd. 856 (2021) 158220, https://doi.org/10.1016/j.jallcom.2020.158220.
[49] J.T. Liang, K.C. Cheng, S.H. Chen, Effect of heat treatment on the phase evolution and mechanical properties of atomized AlCoCrFeNi high-entropy alloy powders, J. Alloys Compd. 803 (2019) 484–490, https://doi.org/10.1016/j.jallcom.2019.06.301.
[50] K.C. Cheng, J.H. Chen, S. Stadler, S.H. Chen, Properties of atomized AlCoCrFeNi high-entropy alloy powders and their phase-adjustable coatings prepared via plasma spray process, Appl. Surf. Sci. 478 (2019) 478–486, https://doi.org/10.1016/j.apsusc.2019.01.203.
[51] T.M. Butler, M.L. Weaver, Oxidation behavior of arc melted AlCoCrFeNi multi-component high-entropy alloys, J. Alloys Compd. 674 (2016) 229–244, https://doi.org/10.1016/j.jallcom.2016.02.257.
[52] T.M. Butler, M.L. Weaver, Influence of annealing on the microstructures and oxidation behaviors of Al8(CoCrFeNi)92, Al15(CoCrFeNi)85, and Al30(CoCrFeNi)70 high-entropy alloys, Metals (Basel) 6 (2016) 222, https://doi.org/10.3390/met6090222.
[53] Q. Shen, X. Kong, X. Chen, Significant transitions of microstructure and mechanical properties in additively manufactured Al–Co–Cr–Fe–Ni high-entropy alloy under heat treatment, Mater. Sci. Eng. A 815 (2021) 141257, https://doi.org/10.1016/j.msea.2021.141257.
[54] T.M. Butler, J.P. Alfano, R.L. Martens, M.L. Weaver, High-temperature oxidation behavior of Al-Co-Cr-Ni-(Fe or Si) multicomponent high-entropy alloys, JOM 67 (2015) 246–259, https://doi.org/10.1007/s11837-014-1185-7.
[55] S. Veselkov, O. Samoilova, N. Shaburova, E. Trofimov, High-temperature oxidation of high-entropic alloys: a review, Materials (Basel) 14 (2021), https://doi.org/10.3390/ma14102595.
[56] M. Garg, H.S. Grewal, R.K. Sharma, H.S. Arora, Improving the high temperature oxidation resistance of high entropy alloy by surface modification, Corros. Rev. 41 (2023) 39–56, https://doi.org/10.1515/corrrev-2022-0011.
[57] M. Tokarewicz, M. Grądzka-Dahlke, Review of recent research on AlCoCrFeNi high-entropy alloy, Metals (Basel) 11 (2021) 1302.
[58] P. Chen, S. Chen, Partial slip contact between a rigid punch with an arbitrary tip-shape and an elastic graded solid with a finite thickness, Mech. Mater. 59 (2013) 24–35, https://doi.org/10.1016/j.mechmat.2012.12.003.
[59] J. Peng, Z. Wang, P. Chen, F. Gao, Z. Chen, Y. Yang, Surface contact behavior of an arbitrarily oriented graded substrate with a spatially varying friction coefficient, Int. J. Mech. Sci. 151 (2019) 410–423, https://doi.org/10.1016/j.ijmecsci.2018.11.032.
[60] P. Chen, S. Chen, Thermo-mechanical contact behavior of a finite graded layer under a sliding punch with heat generation, Int. J. Solids Struct. 50 (2013) 1108–1119, https://doi.org/10.1016/j.ijsolstr.2012.12.007.
[61] C. Peijian, C. Shaohua, P. Juan, Sliding contact between a cylindrical punch and a graded half-plane with an arbitrary gradient direction, J. Appl. Mech. 82 (2015), https://doi.org/10.1115/1.4029781.
[62] A. Meghwal, S. Singh, S. Sridar, W. Xiong, C. Hall, P. Munroe, C.C. Berndt, A.S.M. Ang, Development of composite high entropy-medium entropy alloy coating, Scr. Mater. 222 (2023) 115044, https://doi.org/10.1016/j.scriptamat.2022.115044.
[63] X. Yang, C. Li, M. Zhang, Z. Ye, X. Zhang, M. Zheng, J. Gu, J. Li, S. Li, Dry sliding wear behavior of additively manufactured CoCrWNixAly alloys, Wear. 496–497 (2022) 204285, https://doi.org/10.1016/j.wear.2022.204285.
[64] A. Kolubaev, S. Tarasov, O. Sizova, E. Kolubaev, Scale-dependent subsurface deformation of metallic materials in sliding, Tribol. Int. 43 (2010) 695–699, https://doi.org/10.1016/j.triboint.2009.10.009.
[65] Y.H. Jo, W.-M. Choi, S.S. Sohn, H.S. Kim, B.-J. Lee, S. Lee, Role of brittle sigma phase in cryogenic-temperature-strength improvement of non-equi-atomic Fe-rich VCrMnFeCoNi high entropy alloys, Mater. Sci. Eng. A. 724 (2018) 403–410, https://doi.org/10.1016/j.msea.2018.03.115.
[66] D.-Q. Doan, T.-H. Fang, T.-H. Chen, Structural transformation and strain localization at twin boundaries in Al0.4CoCrFeNi high-entropy alloy, Appl. Surf. Sci. 582 (2022) 152383, https://doi.org/10.1016/j.apsusc.2021.152383.